

# Crew Dragon: On-Orbit Operations

A Simulation of SpaceX's Crew Dragon and the mission of Rendezvous & Docking with the International Space Station

Christopher Covert



AA 279D - Spacecraft Formation-Flying and Rendezvous  
Stanford University

## Revision History

Table 1: Project Changelog

Rev	Changes
PS1	<ul style="list-style-type: none"><li>- Created document</li><li>- Added PS1 material</li></ul>
PS2	<ul style="list-style-type: none"><li>- Implemented PS1 changes</li><li>- Added PS2 material</li><li>- Added List of Figures</li></ul>
PS3	<ul style="list-style-type: none"><li>- Implemented PS2 changes</li><li>- Added error plots</li><li>- Added PS3 material</li></ul>
PS4	<ul style="list-style-type: none"><li>- Added PS4 material</li></ul>
PS5	<ul style="list-style-type: none"><li>- Added PS5 material</li></ul>
PS6	<ul style="list-style-type: none"><li>- Added PS6 material</li></ul>
PS7	<ul style="list-style-type: none"><li>- Added PS7 material</li></ul>
FINAL	<ul style="list-style-type: none"><li>- Added Sections 10,12,13</li><li>- Added Conclusions and Future Work section</li><li>- Added Simulink Model to Appendix B</li></ul>

## Contents

<b>1 Abstract</b>	<b>7</b>
<b>2 Mission Proposals</b>	<b>7</b>
2.1 Primary Candidate: Dragon 2 . . . . .	7
2.2 Secondary Candidate: Starlink Constellation . . . . .	9
<b>3 Orbit Simulation</b>	<b>10</b>
3.1 Keplerian Initial Conditions . . . . .	11
3.2 Inertial Position and Velocity Initial Conditions . . . . .	11
3.3 Unperturbed Orbit Propagation . . . . .	11
3.4 Orbit Propagation with $J_2$ Effects . . . . .	12
3.5 Error Propagation . . . . .	13
3.6 Osculation Disturbances . . . . .	15
3.7 Mean Keplerian Orbital Elements . . . . .	18
3.8 Inconsistencies in Mean vs. Osculating Element Methods . . . . .	21
<b>4 Relative Motion</b>	<b>21</b>
4.1 Initial Conditions . . . . .	21
4.2 Relative Position and Velocity . . . . .	22
4.3 Relative Difference of Absolute Motion . . . . .	23
4.4 Disturbances to Semi-major Axis . . . . .	24
4.5 Impulsive Formation Keeping . . . . .	25
4.6 Discontinuous Inertial Velocity Insertion . . . . .	26
<b>5 Linear Relative Motion</b>	<b>27</b>
5.1 Initial Conditions . . . . .	27
5.2 Rectilinear HCW Propagation . . . . .	28
5.2.1 Integration Constants . . . . .	28
5.2.2 Orbit Propagation . . . . .	29
5.3 Curvilinear HCW Propagation . . . . .	30
5.3.1 Integration Constants . . . . .	30
5.3.2 Orbit Propagation . . . . .	31

<b>6 Linearized Equations of Relative Motion for Eccentric Orbits</b>	<b>32</b>
6.1 Yamanaka-Andersen (YA) and Schaub Integration Constant Differences . . . . .	33
6.2 YA and Schaub Relative Velocity Expressions . . . . .	33
<b>7 Eccentric Orbit Simulation Analysis</b>	<b>34</b>
7.1 Initial Conditions . . . . .	34
7.2 Yamanaka-Andersen (YA) Solution . . . . .	34
7.3 Schaub Solution . . . . .	36
7.4 Numerical Solution . . . . .	38
7.5 Non-zero $\delta a$ Results . . . . .	40
7.6 Highly-Eccentric Results . . . . .	42
<b>8 Perturbed <math>J_2</math> Relative Orbit Motion in Near-Circular Orbits</b>	<b>45</b>
8.1 Initial Conditions . . . . .	45
8.2 Osculating Quasi-Non-Singular Orbital Elements . . . . .	45
8.3 Mean Quasi-Non-Singular Orbital Elements . . . . .	46
8.4 Relative RTN Position . . . . .	47
8.5 Relative Quasi-Non-Singular Orbital Elements . . . . .	47
8.6 Minimum Maneuvers . . . . .	48
8.7 Secular Evolution of the Relative Orbital Elements . . . . .	50
<b>9 Control Law Requirements</b>	<b>52</b>
9.1 R-bar Configuration Mode . . . . .	52
9.2 Rendezvous/Docking Mode . . . . .	53
<b>10 Controller Implementation</b>	<b>53</b>
10.1 Impulsive Reconfiguration . . . . .	54
10.2 Pseudo-Continuous Formation Control . . . . .	54
10.3 Controller Simulation Results . . . . .	55
<b>11 Navigation System Design</b>	<b>59</b>
11.1 Relative State Representation . . . . .	59
11.2 State Prediction Model . . . . .	59
11.3 Covariance Update Matrices . . . . .	59

11.4 Sensor Specifications . . . . .	60
<b>12 Navigation System Implementation</b>	<b>60</b>
<b>13 Filter Integration</b>	<b>62</b>
13.1 Unfiltered Noisy State Control . . . . .	62
13.2 Filtered Noisy State Control . . . . .	65
<b>14 Conclusions and Future Work</b>	<b>67</b>
<b>Appendices</b>	<b>68</b>
<b>A Two Line Element Sets (TLE)</b>	<b>68</b>
<b>B Simulink Control and Filter Model</b>	<b>68</b>
<b>References</b>	<b>69</b>

## List of Figures

1	Unperturbed Orbit Path . . . . .	12
2	Orbit Path with $J_2$ Effects . . . . .	13
3	RTN Position Error [km] . . . . .	14
4	RTN Velocity Error [km/s] . . . . .	15
5	$J_2$ -Affected Osculating Time Histories . . . . .	16
6	$J_2$ -Affected Osculating Time Histories . . . . .	17
7	$J_2$ -Affected Osculating Time Histories . . . . .	18
8	Mean and Osculating Keplerian Orbital Elements . . . . .	20
9	Relative Position and Velocity in 3D . . . . .	22
10	Relative RTN Position and Velocity Vectors . . . . .	23
11	Relative RTN Position and Error . . . . .	23
12	Relative RTN Velocity and Error . . . . .	24
13	Unbounded Relative RTN Position and Error . . . . .	24
14	Unbounded Relative RTN Velocity and Error . . . . .	25
15	$\Delta V_{total}$ vs Orbit Count . . . . .	26
16	Location of Impulse and Corresponding Relative Position . . . . .	27
17	Relative RTN Position and Velocity Vectors . . . . .	29
18	Relative RTN Position and Velocity Vectors . . . . .	30
19	Relative RTN Position and Velocity Vectors . . . . .	31
20	Relative RTN Position and Velocity Vectors . . . . .	32
21	YA Position Solution . . . . .	35
22	YA Velocity Solution . . . . .	36
23	Schaub Position Solution . . . . .	37
24	Schaub Velocity Solution . . . . .	37
25	3D Method Comparison . . . . .	38
26	RTN-Plane Method Position Comparison . . . . .	39
27	RTN-Plane Method Velocity Comparison . . . . .	39
28	3D Method Comparison . . . . .	41
29	RTN-Plane Method Position Comparison . . . . .	41
30	RTN-Plane Method Velocity Comparison . . . . .	42

31	3D Method Comparison . . . . .	43
32	RTN-Plane Method Position Comparison . . . . .	44
33	RTN-Plane Method Velocity Comparison . . . . .	44
34	Osculating Quasi-Non-Singular OE and ROE . . . . .	46
35	Mean Quasi-Non-Singular OE and ROE . . . . .	46
36	RTN-Plane Method Position Comparison [m] . . . . .	47
37	Relative Eccentricity Vector Comparison . . . . .	47
38	Relative Inclination Vector Comparison . . . . .	48
39	Relative Mean Longitude and Semi-Major Axis Comparison . . . . .	48
40	J <sub>2</sub> Perturbed Relative Inclination Comparison . . . . .	50
41	Relative Eccentricity Vector Comparison . . . . .	51
42	Relative Inclination Vector Comparison . . . . .	51
43	Relative Mean Longitude and Semi-Major Axis Comparison . . . . .	52
44	ROE over Mission Duration . . . . .	56
45	True ROE vs Desired ROE for Both Mission Phases . . . . .	56
46	ISS Rendezvous Mission Profile in the RTN Frame . . . . .	57
47	Relative Range over Mission Duration . . . . .	57
48	Individual Drift Phase Ranges . . . . .	58
49	Relative Range over Mission Duration . . . . .	58
50	True vs Measure ROE . . . . .	61
51	3 $\sigma$ Estimate Bounds . . . . .	61
52	Pre-fit and Post-fit Residuals . . . . .	62
53	Noisy ROE Impulsive Control . . . . .	63
54	Range Profile via Unfiltered Noise . . . . .	63
55	Individual Unfiltered Drift Phase Ranges . . . . .	64
56	Filtered $\delta v$ Consumption . . . . .	64
57	Filtered ROE Control . . . . .	65
58	Filtered ROE Residuals . . . . .	65
59	Range Profile via Unfiltered Noise . . . . .	66
60	Individual Unfiltered Drift Phase Ranges . . . . .	66
61	Unfiltered $\delta v$ Consumption . . . . .	67

## 1 Abstract

This report outlines a detailed formation-flying and rendezvous simulation which summarizes the following fundamental Guidance, Navigation, and Control (GNC) requirements: Keplerian orbital mechanics and orbital perturbations; the general relative motion problem; linear formation-flying dynamics and control; impulsive station-keeping and reconfiguration; high-order relative motion equations; formulation of relative motion using orbital elements; perturbation-invariant formations; nonlinear formation control; low-thrust propulsion for formation flying; relative navigation using GNSS and optical navigation.

The generation of this report is supported in part by SpaceX's Paul Forquera (Director of GNC) and Justin Smith (Manager of Dragon GNC) to coincide with an Associate Engineering position to take place during the Summer of 2018 under the supervision of Dragon 2 GNC managers for the purpose of on-orbit operations with the International Space Station (ISS).

## 2 Mission Proposals

The following mission proposals represent two of SpaceX's leading satellite-based high-profile missions. Due to the lack of publicly available information on Crew Dragon mission specifications, analogies will be drawn from Dragon CRS-14 whenever possible to provide an accurate estimate of orbit planning based upon mission objectives and absolute/relative orbit parameters.

### 2.1 Primary Candidate: Dragon 2

The following information is taken from the launch of Dragon CRS-14 with the accompanying TLE in Appendix A:

- Mission Name and Operator
  - SpaceX CRS-14, USA
  - Contracted: NASA, Flown: SpaceX
- Mission Objectives
  - Scientific Investigations Cargo
    - RemoveDebris Satellite:a small satellite mission by Surrey NanoSatellite Technology Ltd. under a European Union Framework 7 research project to develop and fly a low-cost demonstrator for the key aspects of Active Debris Removal missions on a quest to address the growing space debris problem. The 100-Kilogram, cube-shaped satellite - the largest deployed from the International Space Station to date (2018) - will demonstrate active debris removal techniques by releasing, tracking and capturing two small CubeSats called DebrisSATS, in the process demonstrating different rendezvous, capture and deorbiting techniques to evaluate their feasibility for operational debris removal missions of the future.
    - MISSE Flight Facility:The Materials on ISS Experiment - Flight Facility (MISSE-FF) builds on the success of the original MISSE Passive Experiment Container concept which consisted of smaller and larger sample plates containing a variety of surface materials for exposure to the space environment outside the International Space Station for varying durations to inform

satellite designers on how different materials degrade over time. The MISSE-FF project created a platform capable of holding 14 exchangeable sample modules for powered & heated payloads as well as passive experiments.

- ASIM: the Atmosphere-Space Interactions Monitor, is an ESA science instrument taking up residence outside the Columbus Module of the International Space Station to study Transient Luminous Events (TLEs) in Earth’s upper atmosphere like Blue Jets, Red Sprites and Elves via a suite of cameras and photometers sensitive in a broad wavelength range to reveal previously unknown details of the electrical and chemical processes ongoing where the atmosphere and space interact.
- PFCS Spare: The third Trunk Payload riding on the Dragon SpX-14 mission is not a science/utilization instrument like its two companions but a potentially critical spare part for the Space Station’s Thermal Control System. The Pump Flow Control Subassembly, PFCS for short, is a critical component of the ISS Photovoltaic Thermal Control System (PVTCS) in that it routes ammonia coolant to transport heat from the various electrical assemblies located within the Integrated Equipment Assembly to a Photovoltaic Radiator where it is dissipated into space.

- Number and Type of Satellites

- One CRS Dragon C110.2 for ISS Resupply
  - One International Space Station

- Absolute and Relative Orbit Parameters

- Reference system: Geocentric
  - Regime: Low Earth
  - Launch date: 2 April 2018, 20:30:38 UTC
  - Perigee Altitude: 410.1 km
  - Apogee Altitude: 412.7 km
  - Period: 92.6 minutes
  - More information available in Section 3.1

- Basic Description of Functioning/Scientific Principle

- The Dragon spacecraft rendezvoused with the ISS April 4th, 2018 in order to complete a scheduled resupply mission. After an r-bar rendezvous maneuver, it was captured by Canadarm2 at 10:40 UTC and was berthed to the Harmony module at 13:00 UTC. It is scheduled to remain there for approximately one month before de-orbiting and returning to Earth [2].

- Key GNC Requirements

- For the purpose of on-orbit navigation, Dragon has a suite of Inertial Measurement Units (IMU), GPS Systems, Iridium Recovery Beacons, and Star Trackers. Both the IMUs and star trackers have an accuracy of  $0.004^\circ$  or smaller. The threshold of attitude control is also  $0.012^\circ$  on each axis in station-keeping Mode [4]. As a Dragon module, the following GNC requirements are required for successful rendezvous: GNC bay door deploys, exposing the GNC sensor suite; star tracker attitude initiation works as expected; TDRSS S-band telemetry and commanding works

as expected; demonstrates precision R-bar arrival at 350 m below the ISS; initializes proximity sensors (LIDARs and thermal imagers) and converges a solution for range and range rate before proceeding; demonstrates hold and retreats commanded by the ISS crew; enters free drift at 10 m from the ISS with minimal vehicle body rates; successfully berths to Node 2 Nadir[6].

- Classification
  - Nadir Berthing Rendezvous

## 2.2 Secondary Candidate: Starlink Constellation

The following information is taken from the launch of Tintin A & B with the accompanying TLEs in Appendix A:

- Mission Name and Operator
  - SpaceX Starlink, USA
- Mission Objectives
  - Develop a low-cost, high-performance satellite bus and requisite customer ground transceivers to implement a new space-based Internet communication system. Secondary objectives include the sale of satellites that use the same satellite bus that may be used for scientific or exploratory purposes in order to fund future Mars transport projects. [7]
- Number and Type of Satellites
  - Two Smallsat-class communication satellites Tintin A & B
- Absolute and Relative Orbit Parameters
  - Both:
    - Reference system: Geocentric
    - Regime: Low Earth
    - Orbit Type: Sun-Synchronous
    - Launch date: 22 February 2018
  - Tintin A
    - Perigee Altitude: 504.2 km
    - Apogee Altitude: 526.5 km
    - Period: 94.8 minutes
    - Epoch: 15 April 2018, 15:18:56 UTC.
    - $a = 6886.14$  km
    - $e = 0.0016$
    - $i = 97.4630^\circ$
    - $\Omega = 114.1702^\circ$

- $\omega = 97.6203^\circ$
- $M_0 = 262.6859^\circ$
- Tintin B
  - Perigee: 504.1 km
  - Apogee: 526.2 km
  - Period: 94.8 minutes
  - Epoch: 15 April 2018, 5:12:45 UTC.
  - $a = 6886.35$  km
  - $e = 0.0016$
  - $i = 97.4562^\circ$
  - $\Omega = 114.6986^\circ$
  - $\omega = 91.5260^\circ$
  - $M_0 = 268.7829^\circ$

- Basic Description of Functioning/Scientific Principle

- The satellites will employ optical inter-satellite links and phased array beam forming and digital processing technologies in the Ku- and Ka band. Ka- and Ku-band satellites will orbit at an altitude of 1,200 km (750 miles), and V-band satellites will orbit lower at 210 miles (340 km.). The proposed Starlink constellation includes 4,425 higher orbit satellites and 7,518 lower orbit satellites using a peer-to-peer protocol simpler than IPv6. Since each satellite would orbit at 1/30 of geostationary orbits, they offer practical latencies around 25 to 35 ms, comparable to currently existing cable or fiber networks [8].

- Key GNC Requirements

- Not much is known about the Tintin A & B satellites or the Starlink Constellation project due to the nature of these demonstrations as technical proofs of concept in a market that is growing to be increasingly more competitive. Therefore, information regarding the GNC of these satellites is not publicly available.

- Classification

- Communication Satellite Constellation

### 3 Orbit Simulation

The following orbit simulation and data analysis was conducted on Dragon CRS-14 for a berthing maneuver to the ISS. Whereas Crew Dragon will forgo berthing for a docking approach, CRS-14 provides an accurate measure of orbit parameters that Crew Dragon will be designed to emulate. All initial conditions were derived from the TLE in Appendix A.

### 3.1 Keplerian Initial Conditions

The initial conditions of the simulation are provided as a set of Keplerian orbital elements and an initial epoch date and time. Since a TLE for this mission is available, initial launch time is replaced with an active epoch time.

Therefore, although the mission has a launch date of 2 April 2018, 20:30:38 UTC, all initial conditions are taken from the TLE at Epoch: 15 April 2018, 12:27:43 UTC.

$$a = 6782.42 \text{ km}$$

$$e = 0.0002.42$$

$$i = 51.6438^\circ$$

$$\Omega = 331.1221^\circ$$

$$\omega = 355.8915^\circ$$

$$M_0 = 76.9789^\circ$$

### 3.2 Inertial Position and Velocity Initial Conditions

By treating these initial Keplerian elements as osculating quantities, computing the corresponding initial position and velocity in the appropriate inertial frame (Earth-Centered Inertial for an Earth-orbiting mission), leads to the following vectors:

$$r_0^{ECI} = [3689.667, 2558.674, 5082.996]' \text{ [km]}$$

$$v_0^{ECI} = [-5.739, 4.764, 1.769]' \text{ [km/s]}$$

### 3.3 Unperturbed Orbit Propagation

For an unperturbed system, vehicle dynamics follow a simple second-order non-linear ODE with zero disturbance forces present. This ODE represents the gravitational acceleration felt on the vehicle in ideal conditions (homogeneous spherical Earth mass model with  $M_1 \ll M_2$  and no external forces). Using the initial inertial states as provided in section 3.2, the following equation can be numerically integrated [1]:

$$\ddot{\mathbf{r}} + \frac{\mu \mathbf{r}}{r^3} = \mathbf{0}$$

By neglecting any perturbations beyond the two-body spherical gravity force acting on the orbit, the following orbit path was produced over a span of 100 complete orbits with a numerical integration step size of 1 second.

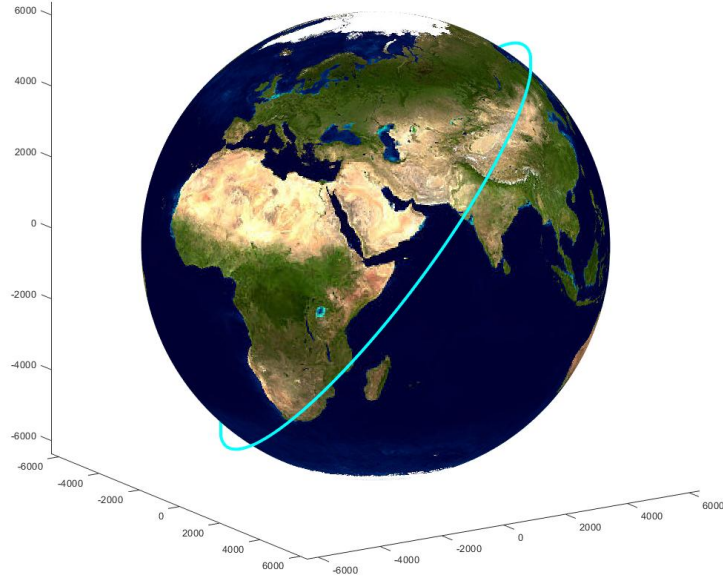


Figure 1: Unperturbed Orbit Path

### 3.4 Orbit Propagation with $J_2$ Effects

By considering  $J_2$  effects from Earth oblateness, small disturbances can be introduced into the numerical integration to produce a non-constant orbit path. The governing dynamics then introduce non-zero forces proportional to  $J_2$  as prescribed below [1]:

$$\begin{aligned}\ddot{X} &= -\frac{\mu X}{r^3} \left[ 1 - \frac{3}{2} J_2 \left( \frac{R_e}{r} \right)^2 \left( 5 \frac{Z^2}{r^2} - 1 \right) \right] \\ \ddot{Y} &= -\frac{\mu Y}{r^3} \left[ 1 - \frac{3}{2} J_2 \left( \frac{R_e}{r} \right)^2 \left( 5 \frac{Z^2}{r^2} - 1 \right) \right] \\ \ddot{Z} &= -\frac{\mu Z}{r^3} \left[ 1 - \frac{3}{2} J_2 \left( \frac{R_e}{r} \right)^2 \left( 5 \frac{Z^2}{r^2} - 3 \right) \right]\end{aligned}$$

The following orbit path was run over the same parameters as Figure 1 with the addition of  $J_2$  effects.

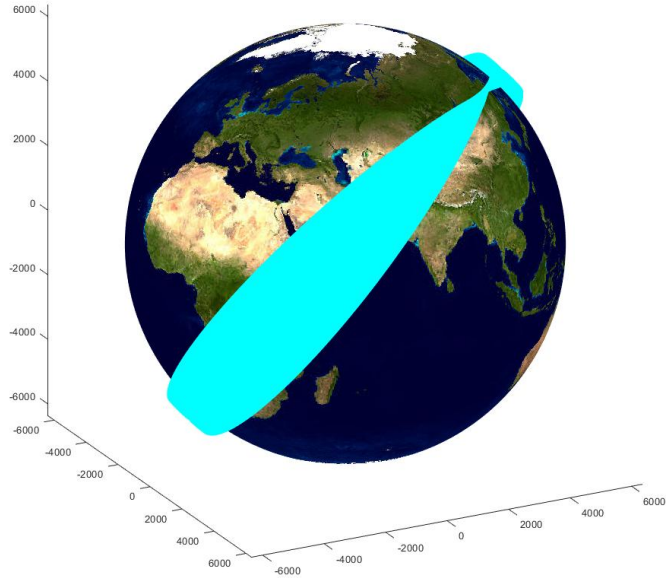


Figure 2: Orbit Path with  $J_2$  Effects

### 3.5 Error Propagation

By comparing the state output from the unperturbed numerical integration against an analytical Keplerian propagation, the accuracy of the integrator can be demonstrated. The error in absolute position and inertial velocity expressed in the local vertical, local horizontal (RTN) coordinate system can be seen below for a simulation over a span of 10 complete orbits with a numerical integration step size of 1/100,000th of an orbit period.

As the error in the system propagates over the length of the simulation, error accumulated over the span of 10 orbits was shown to accuracy drift and potential divergence.

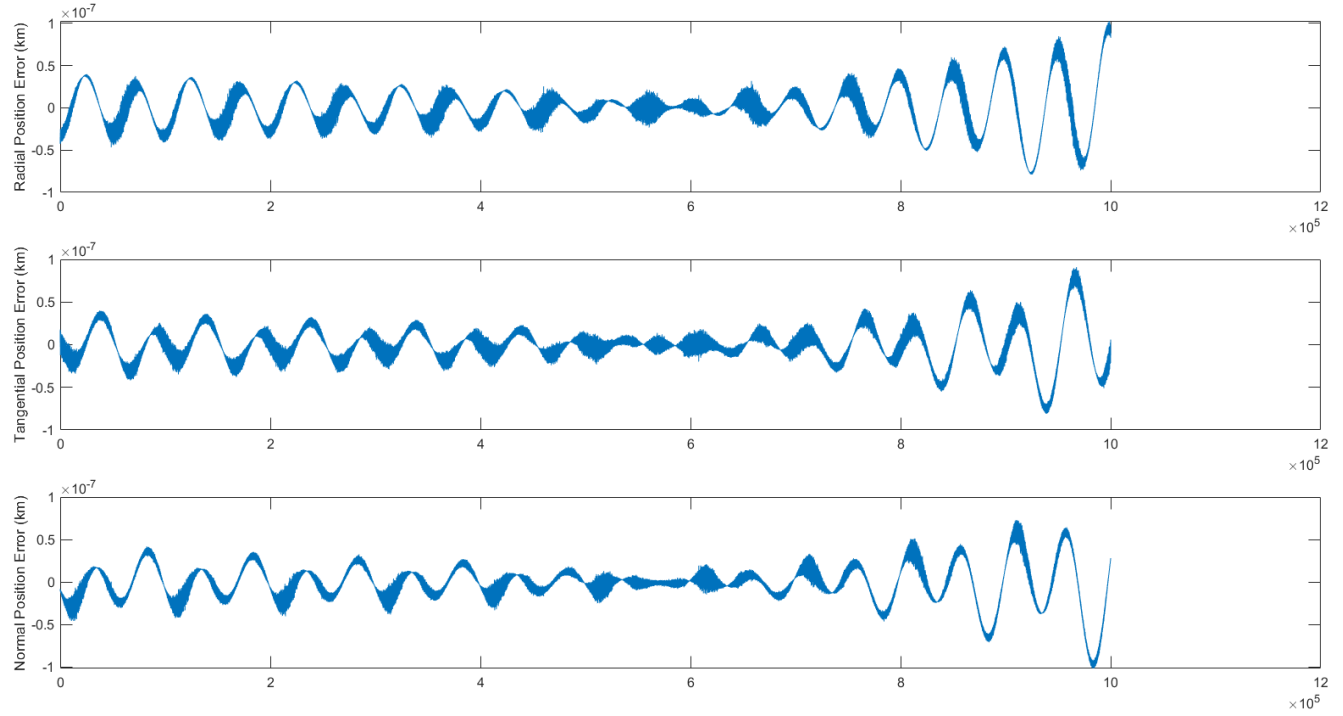


Figure 3: RTN Position Error [km]

As seen in the vertical axis of this plot, the error over 10 orbits is scaled to  $10^{-7}$  km, or 0.1 mm. Therefore, the numerically integrated position vector,  $r^{RTN}$ , is accurate and has negligible error propagation over 10 orbits.

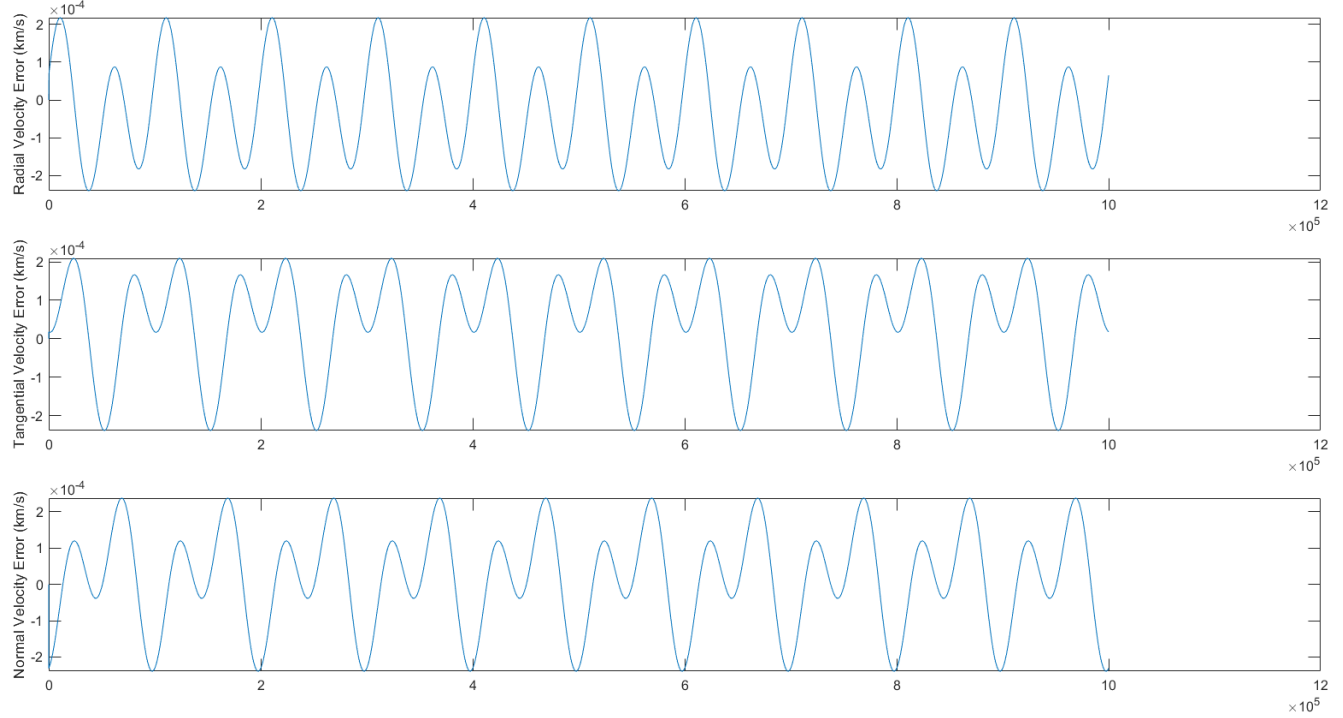


Figure 4: RTN Velocity Error [km/s]

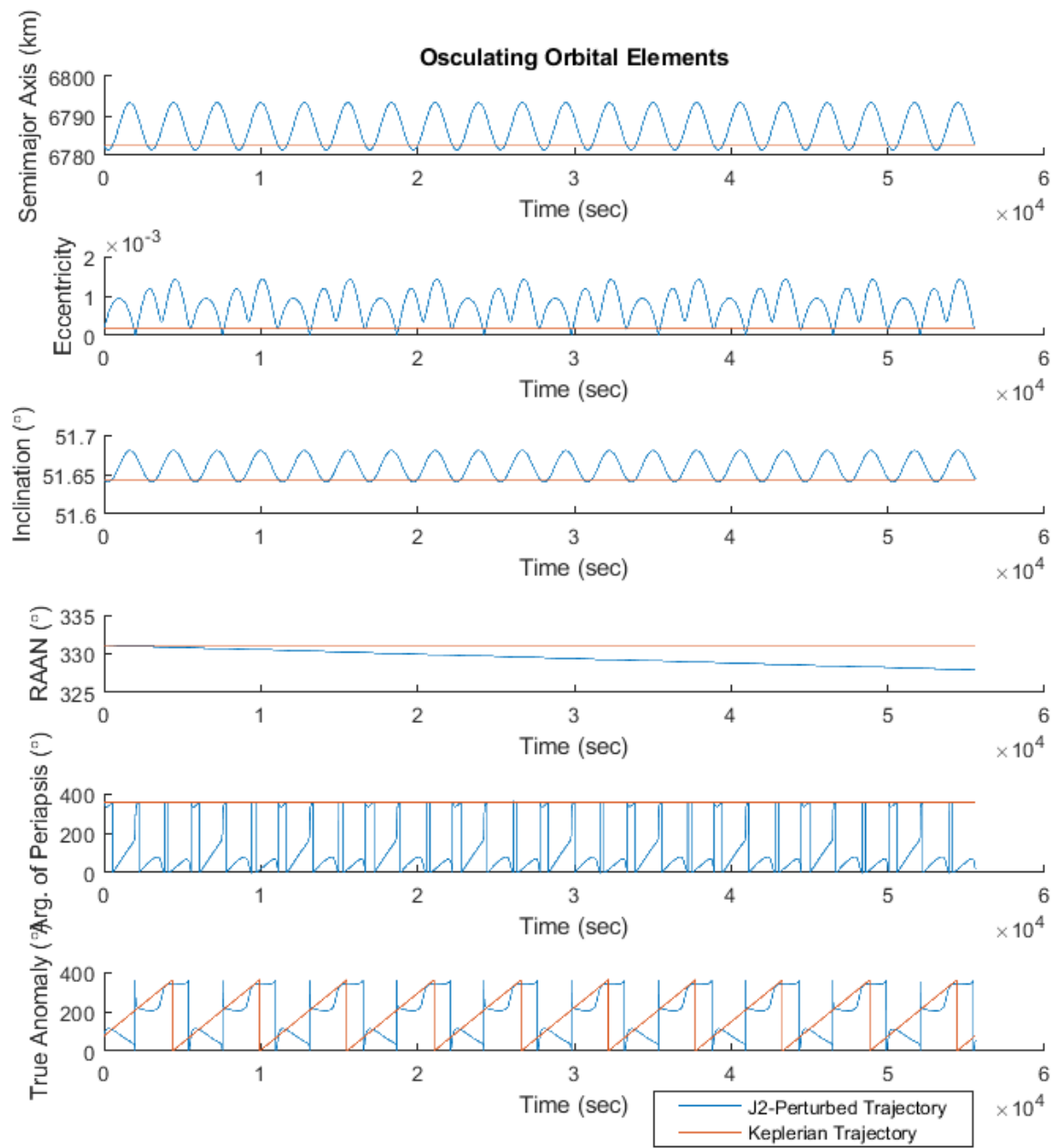
In this plot, the error over 10 orbits is scaled to  $10^{-4}$  km, or 1 cm. Therefore, although larger than the positional error, the numerically integrated velocity vector,  $v^{RTN}$ , is also accurate and has negligible error propagation over 10 orbits.

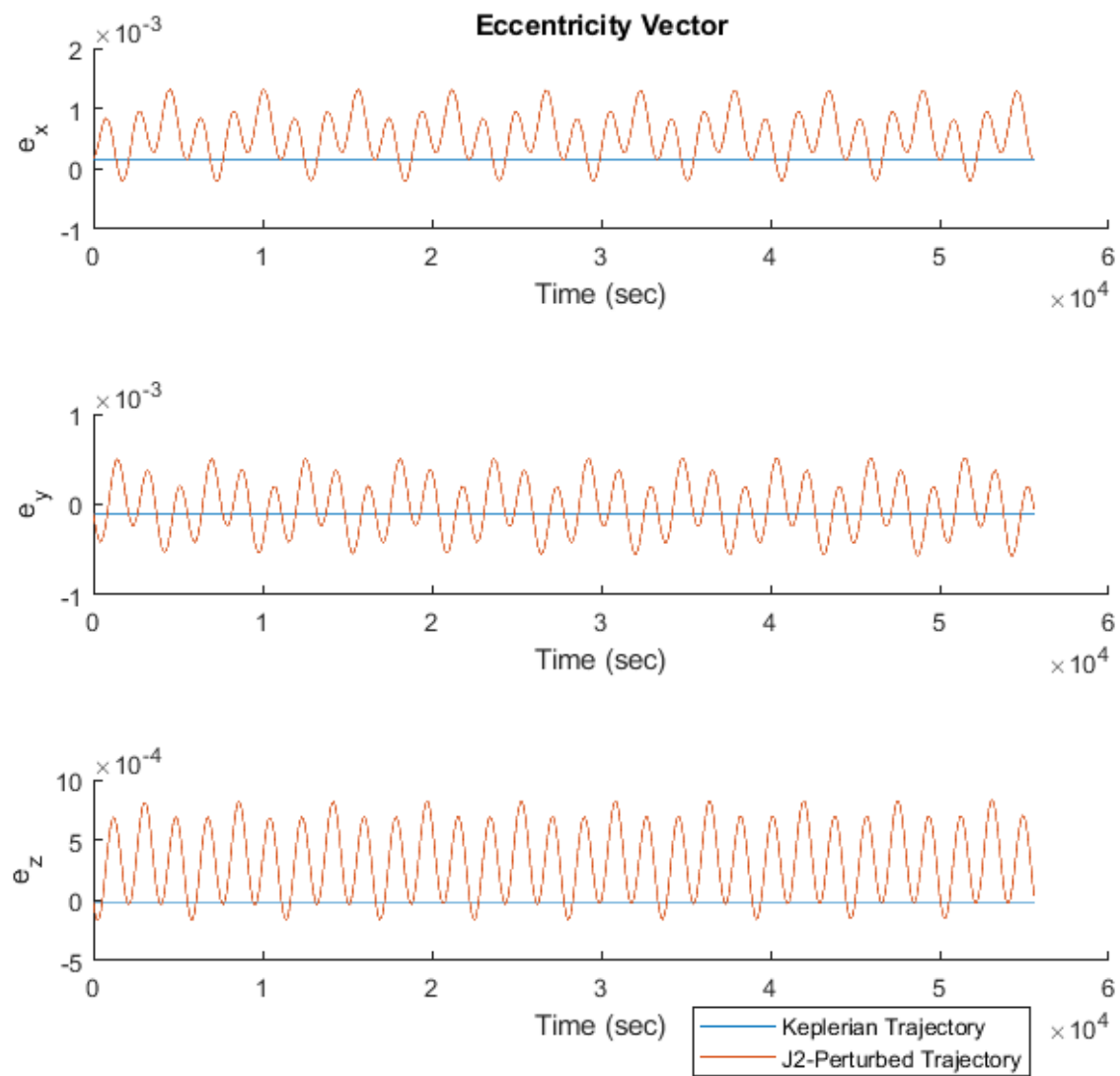
### 3.6 Osculation Disturbances

When excluding  $J_2$  effects, it can be seen that the disturbance-free time history for the Keplerian orbital elements ( $a, e, i, \Omega, \omega$ ), the magnitude of the angular momentum, and the specific mechanical energy are all constant. The only non-constant value is the true anomaly, which is monotonically increasing (modulo  $360^\circ$ ).

The following was run over a span of 10 complete orbits with a numerical integration step size of 1 second.

With the addition of  $J_2$  effects, the oblateness of the Earth provides a small disturbance in the gravitational acceleration of the vehicle that is no longer constant, but has a low frequency mode relating to its orbit and relative position to the equator.

Figure 5:  $J_2$ -Affected Osculating Time Histories

Figure 6:  $J_2$ -Affected Osculating Time Histories

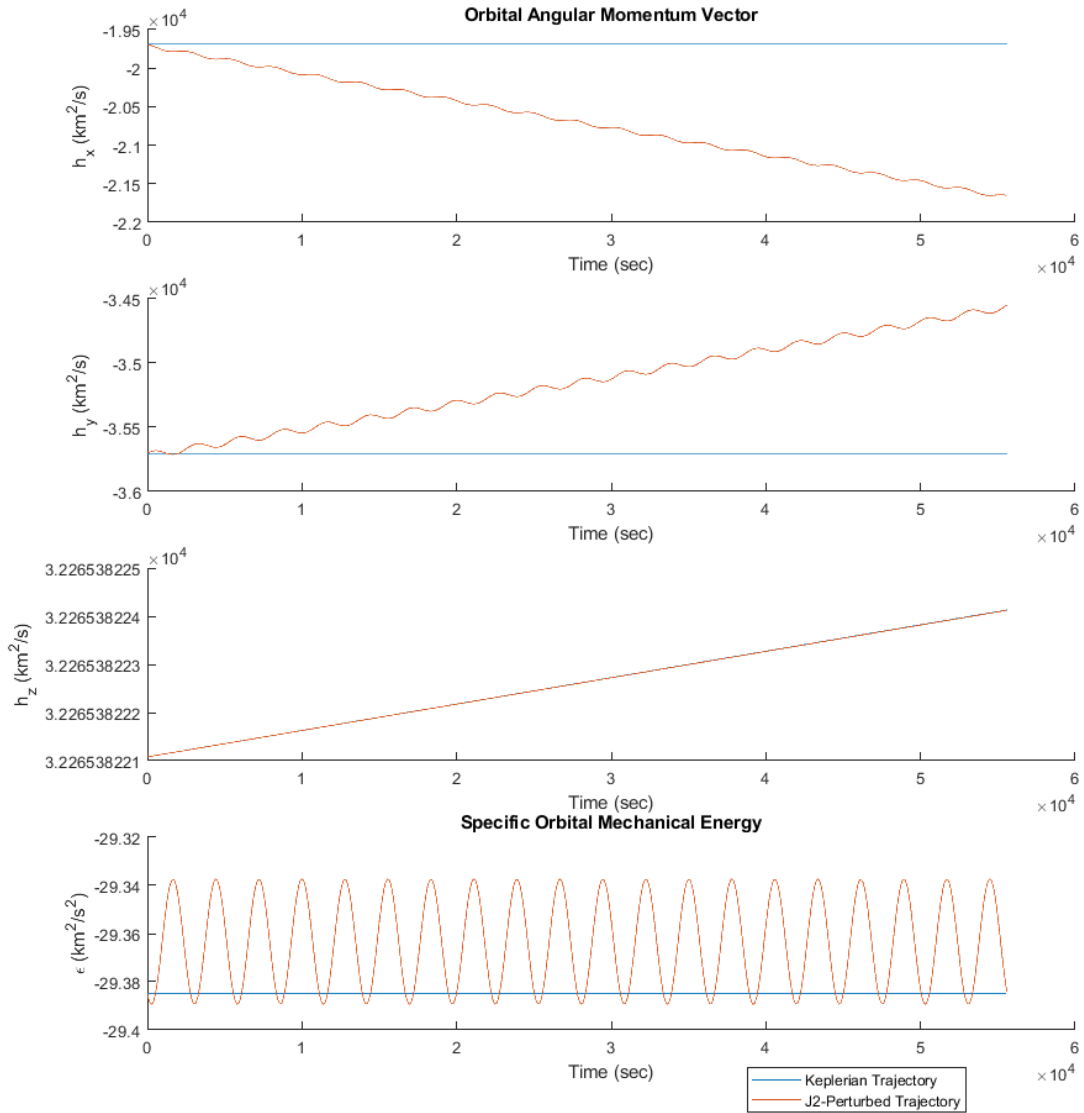


Figure 7:  $J_2$ -Affected Osculating Time Histories

Although difficult to see on such a timescale, these results are as expected from the results of averaging theory (discussed in the following section), where the semimajor axis, eccentricity, and inclination only experience periodic changes, while the RAAN, argument of periapsis, and true anomaly undergo both periodic and secular effects.

### 3.7 Mean Keplerian Orbital Elements

By using Averaging Theory as a comparison to the osculating orbital elements from Figure 6, the following simplified first-order linear ODE's can be used to propagate the mean Keplerian orbital elements with J2 effects [1]:

$$\begin{aligned}
\frac{d\bar{a}}{dt} &= 0 \\
\frac{d\bar{e}}{dt} &= 0 \\
\frac{d\bar{i}}{dt} &= 0 \\
\frac{d\bar{\Omega}}{dt} &= -\frac{3}{2} J_2 \left( \frac{R_e}{\bar{p}} \right)^2 \bar{n} \cos \bar{i} \\
\frac{d\bar{\omega}}{dt} &= \frac{3}{4} J_2 \left( \frac{R_e}{\bar{p}} \right)^2 \bar{n} (5 \cos^2 \bar{i} - 1) \\
\frac{d\bar{M}_0}{dt} &= \frac{3}{4} J_2 \left( \frac{R_e}{\bar{p}} \right)^2 \bar{n} \bar{\eta} (3 \cos^2 \bar{i} - 1)
\end{aligned}$$

It should be noted that the inputs for this system are mean elements, not instantaneous ones. The following plot compares the osculating orbital elements (solid, red) to the expected mean Keplerian orbital elements with  $J_2$  effects (dotted, black).

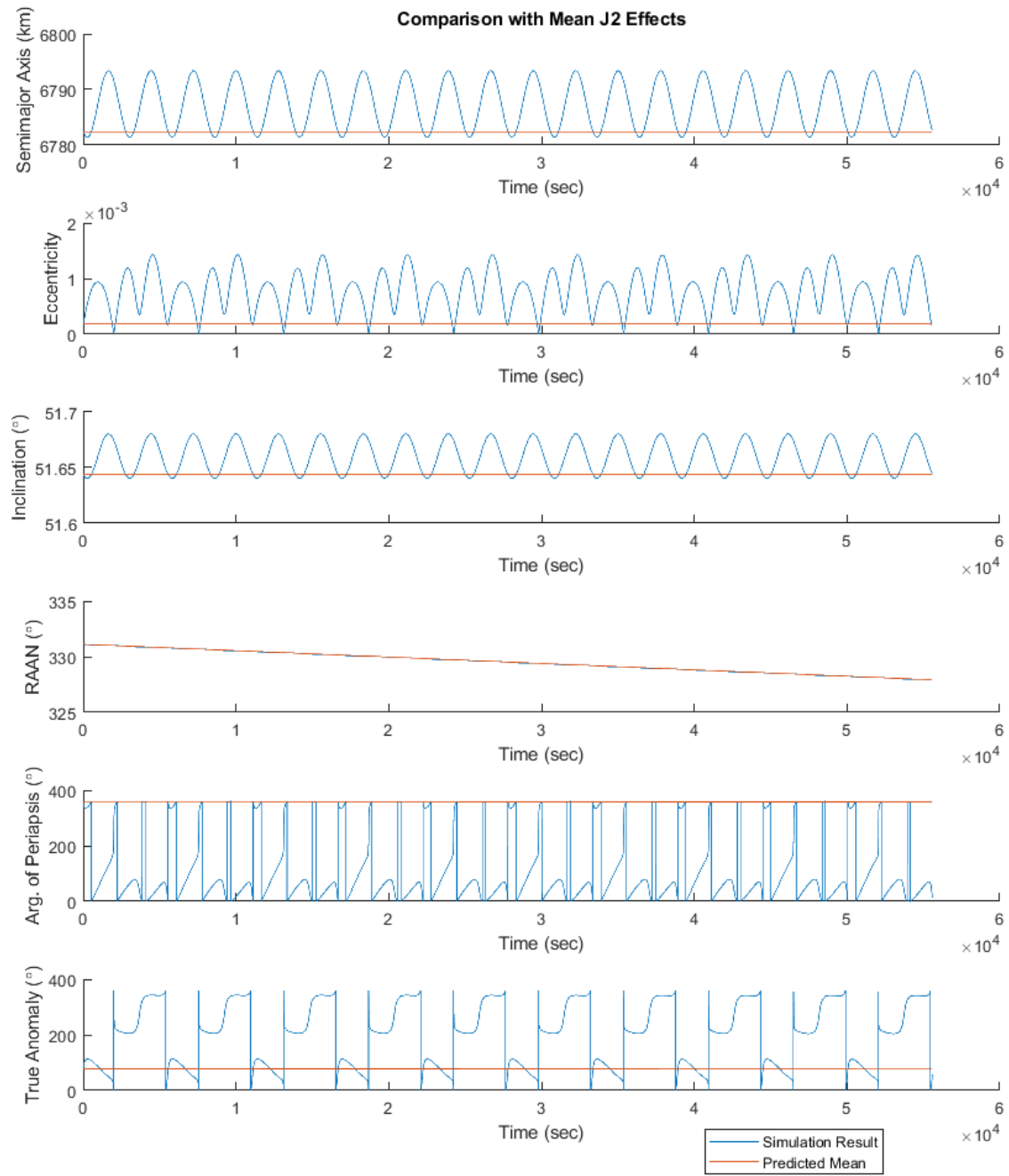


Figure 8: Mean and Osculating Keplerian Orbital Elements

Clearly, the mean orbital elements represent the mean of the osculating orbital elements as expected from Averaging Theory.

### 3.8 Inconsistencies in Mean vs. Osculating Element Methods

It is possible to encounter inconsistencies when comparing osculating and mean orbital elements due the initialization procedure. In fact, one uses osculating states as inputs and provides osculating states as outputs, whereas the other uses mean states as inputs and provides mean states as outputs.

Since the mean states cannot be calculated without the osculating orbit, it is possible to run a simulation of a single orbit to provide enough information to initialize the mean states. Therefore, if computational costs are a factor, the calculation of the osculating orbital elements must only be computed for one orbit and the mean Keplerian orbital elements may be used for the remainder of the calculation. It should be noted, however, that the stronger the  $J_2$  effects are on the orbit, the greater the standard deviation in the osculating terms from the mean terms (which increasing instantaneous error).

In order to convert between osculating and mean orbital elements, a few methods are available: Brouwer's Satellite Theory, Short-Period Kozai-Izsak theory, and Eckstein-Ustinov theory to name a few (variations on PLEs and GVEs).

## 4 Relative Motion

### 4.1 Initial Conditions

The chief orbit in this simulation is taken directly from the initial conditions of the prior simulation in Section 3.1:

Chief:

$$\begin{aligned} a &= 6782.42 \text{ km} \\ e &= 0.0002.42 \\ i &= 51.6438^\circ \\ \Omega &= 331.1221^\circ \\ \omega &= 355.8915^\circ \\ M_0 &= 76.9789^\circ \end{aligned}$$

From the Chief orbit, small variations were applied to the Keplerian orbital elements to produce a Deputy orbit with a  $1^\circ$  change in inclination,  $\Omega$ , and  $\omega$ .

Deputy:

$$\begin{aligned} a &= 6782.42 \text{ km} \\ e &= 0.0002.42 \\ i &= 52.6438^\circ \\ \Omega &= 332.1221^\circ \\ \omega &= 356.8915^\circ \\ M_0 &= 76.9789^\circ \end{aligned}$$

These changes in orbital elements are a valid set of initial conditions due to the relation of relative position to the value of  $r_0$ , satisfying:

$$\|\vec{\rho}\| \leq 0.001 \|\vec{r}_0\|$$

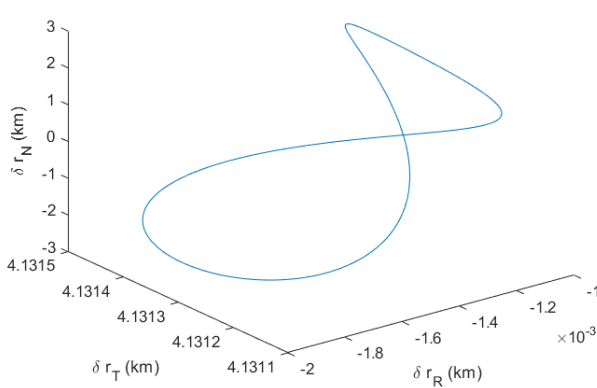
## 4.2 Relative Position and Velocity

A numerical integration of the nonlinear equations of relative motion can be performed on Eqns (4.17) - (4.19) from [1]:

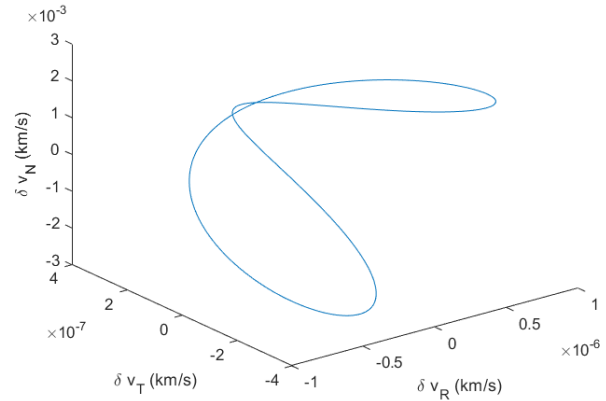
$$\begin{aligned}\ddot{x} - 2\dot{\theta}_0\dot{y} - \ddot{\theta}_0^2 y - \dot{\theta}_0^2 x &= -\frac{\mu(r_0 + x)}{[(r_0 + x)^2 + y^2 + z^2]^{\frac{3}{2}}} + \frac{\mu}{r_0^2} + d_x + u_x \\ \ddot{y} + 2\dot{\theta}_0\dot{x} + \ddot{\theta}_0x - \dot{\theta}_0^2 y &= -\frac{\mu y}{[(r_0 + x)^2 + y^2 + z^2]^{\frac{3}{2}}} + d_y + u_y \\ \ddot{z} &= -\frac{\mu z}{[(r_0 + x)^2 + y^2 + z^2]^{\frac{3}{2}}} + d_z + u_z\end{aligned}$$

From this integration, relative position and velocity vectors can be propagated in the rotating RTN frame with origin at the chief spacecraft.

The following plots were produced over 10 orbits with a step size of 5 seconds.



(a) Relative Position (3D)



(b) Relative Velocity (3D)

Figure 9: Relative Position and Velocity in 3D

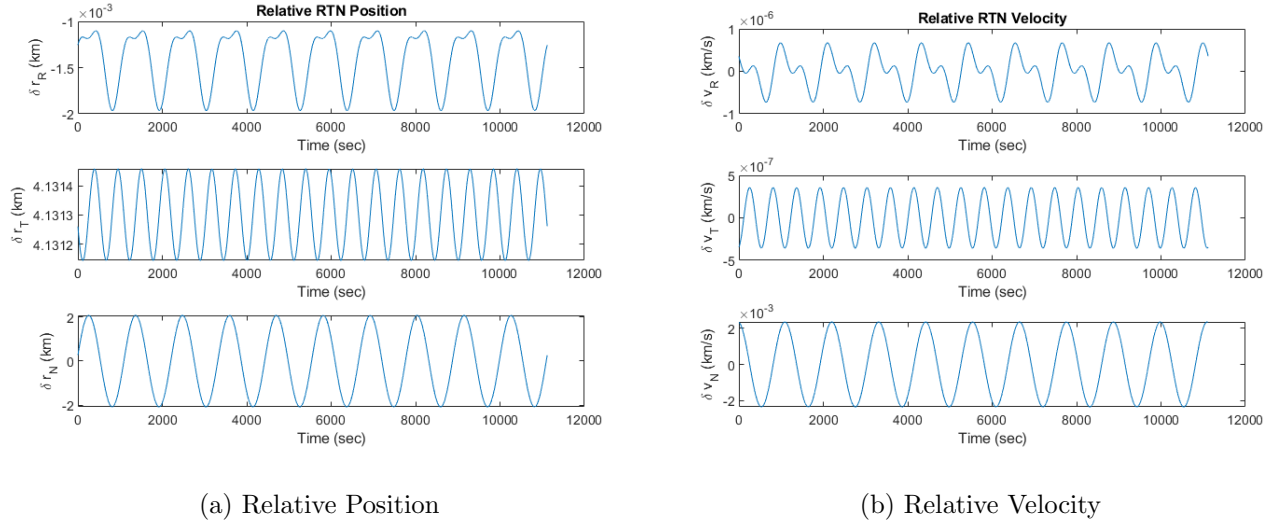


Figure 10: Relative RTN Position and Velocity Vectors

### 4.3 Relative Difference of Absolute Motion

A verification of the numerical integrator can be performed by differencing the results of differential equations of absolute motion for both the chief and deputy orbits.

Below is a plot of the data, showing that both simulations overlap and that the numerical integration of the previous section is held to an order of numerical error, therefore verifying the validity of the integration method.

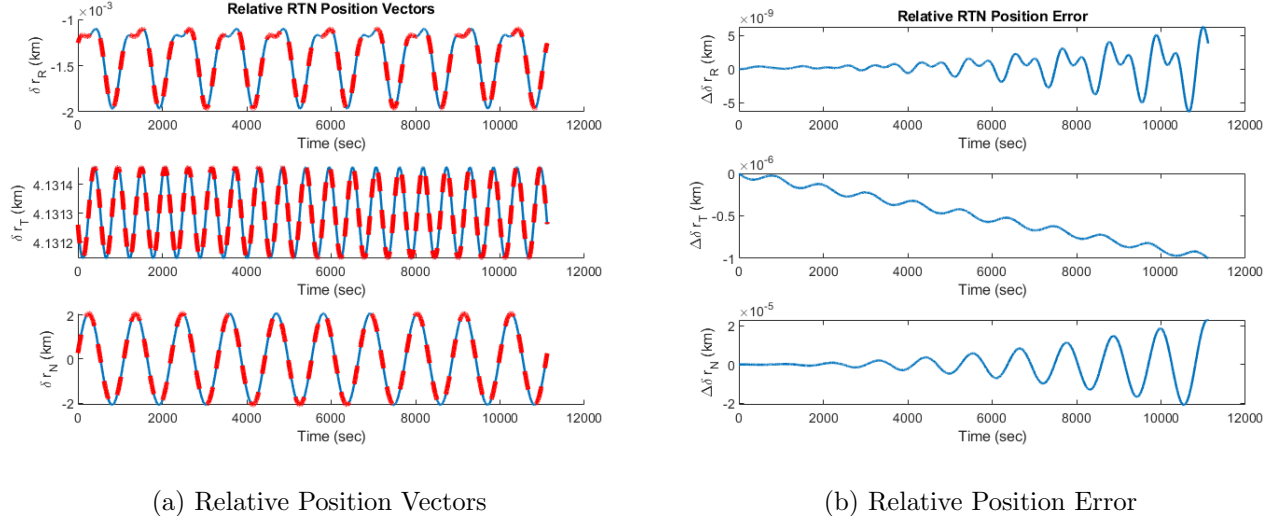
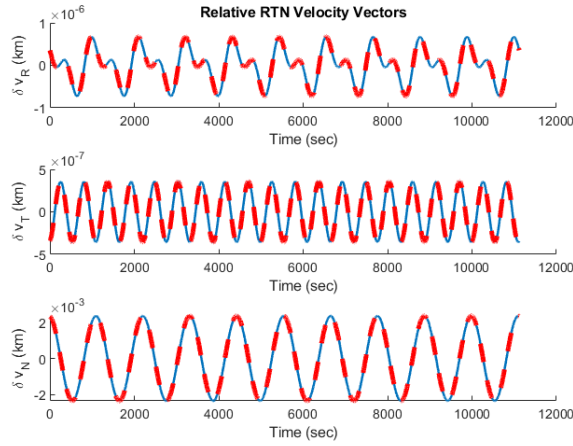
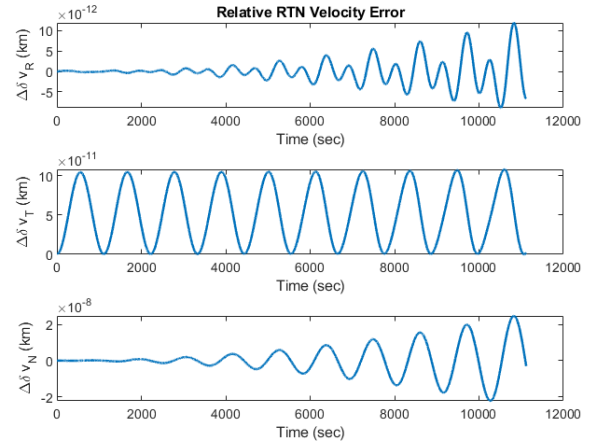


Figure 11: Relative RTN Position and Error



(a) Relative Velocity Vectors

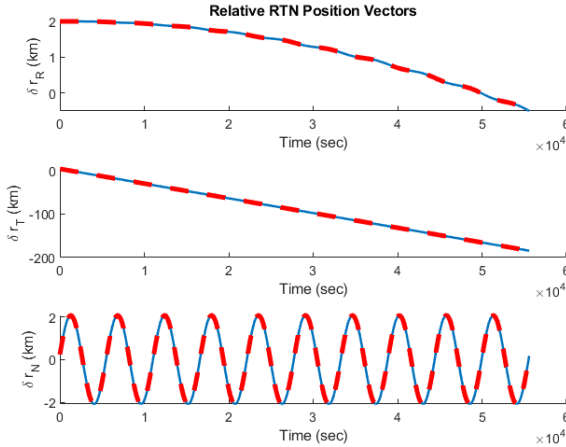


(b) Relative Velocity Error

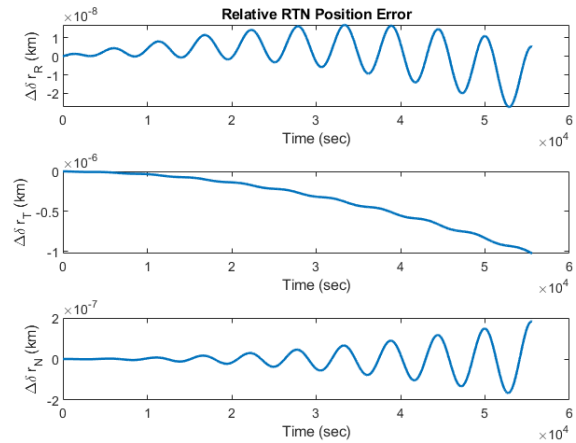
Figure 12: Relative RTN Velocity and Error

#### 4.4 Disturbances to Semi-major Axis

By adding a relative disturbance to the semi-major axis, a difference in mechanical energy is induced, thus leading to a locally unbounded relative motion. With a  $\Delta a$  of 2 km, the following unbounded solution is produced.



(a) Relative Position Vectors



(b) Relative Position Error

Figure 13: Unbounded Relative RTN Position and Error

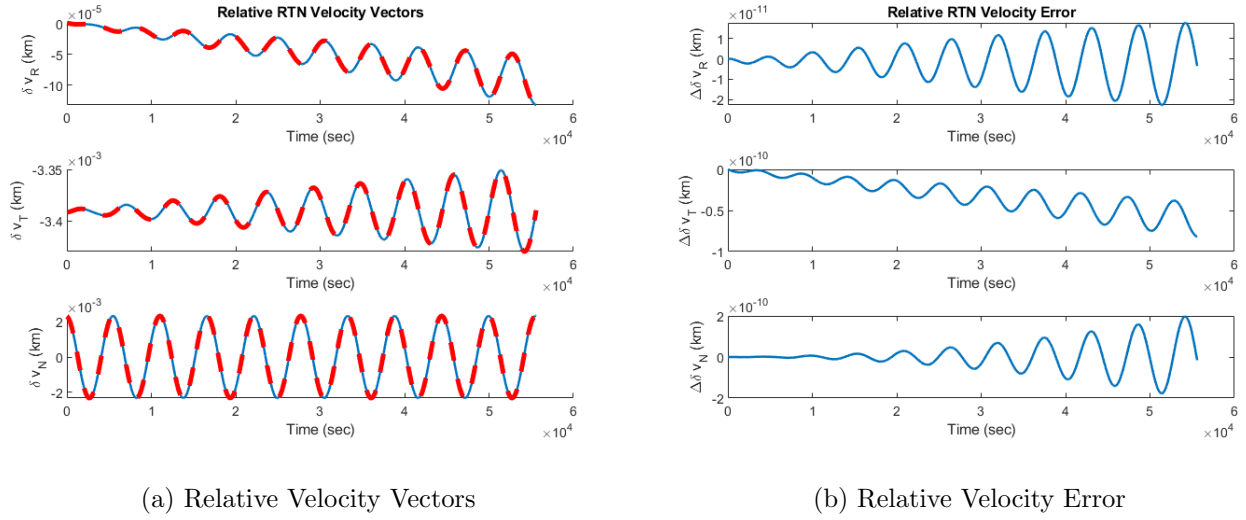


Figure 14: Unbounded Relative RTN Velocity and Error

#### 4.5 Impulsive Formation Keeping

In order to re-establish a bounded periodic relative motion between deputy and chief orbits, the following equations may be used to calculate  $\Delta V$ :

$$\begin{aligned} v_x^- &= \dot{x}^-(t_i) - \dot{\theta}_0^-(t_i)y(t_i) + \dot{r}_0^-(t_i) \\ v_y^- &= \dot{y}^-(t_i) + \dot{\theta}_0^-(t_i)[x(t_i) + r_0(t_i)] \\ v_z^- &= \dot{z}^-(t_i) \\ r_1 &= \sqrt{[r_0(t_i) + x(t_i)]^2 + y^2(t_i) + z^2(t_i)} \end{aligned}$$

$$\frac{\Delta v_x^*}{v_x^-} = \frac{\Delta v_y^*}{v_y^-} = \frac{\Delta v_z^*}{v_z^-} = -1 + \frac{1}{v_1^-} \sqrt{\frac{\mu(2a_0 - r_1)}{a_0 r_1}}$$

$$\Delta v^* = \sqrt{(\Delta v_x^*)^2 + (\Delta v_y^*)^2 + (\Delta v_z^*)^2} = v_1^- - \sqrt{\frac{\mu(2a_0 - r_1)}{a_0 r_1}}$$

ΔV Parameters	
$\Delta V_x$	6.833e-07 km/s
$\Delta V_y$	-1.129e-03 km/s
$\Delta V_z$	-3.419e-07 km/s

Table 2: Minimum-Fuel Impulse ΔV Maneuver

#### 4.6 Discontinuous Inertial Velocity Insertion

The maneuver should take place on the the minimum impulse value in order to save fuel for future maneuvers. In the following plot of  $\Delta V_{total}$  vs Orbit Count, it can be seen where the best position to fire the impulse lies around the fifth orbit:

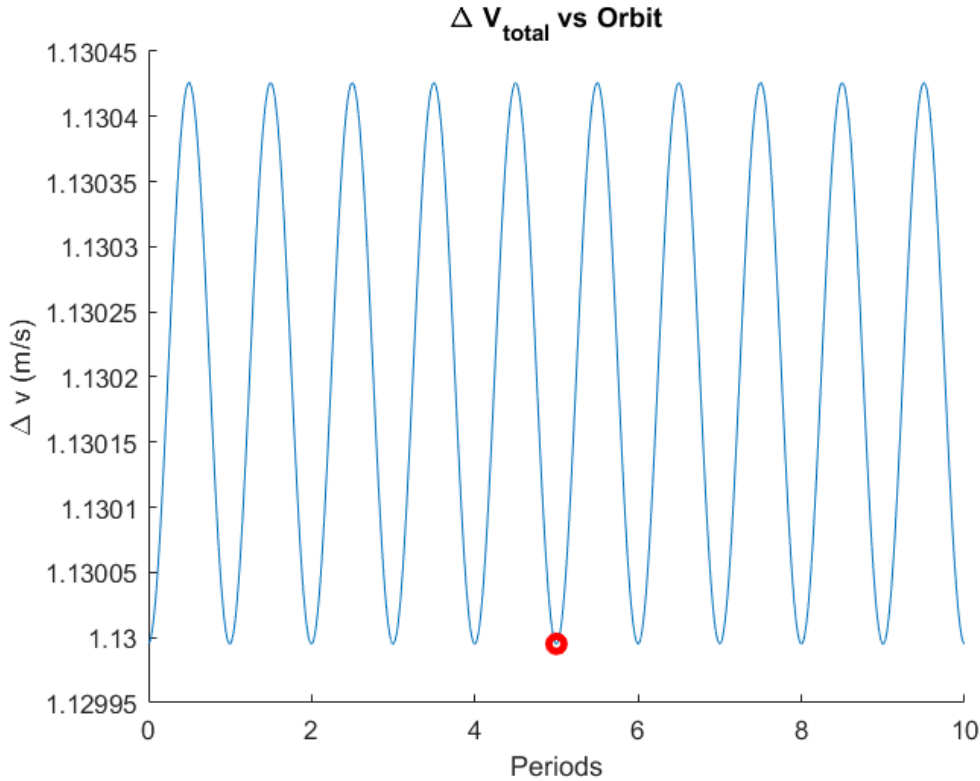


Figure 15:  $\Delta V_{total}$  vs Orbit Count

From this plot, it can be seen that the first viable location for the impulse is near the initial conditions, but on the fifth orbit. By injecting a discontinuity of  $\Delta V$ /stepsize as  $u$  into the equations of relative motion, a re-establishment of bounded periodic motion may be induced.

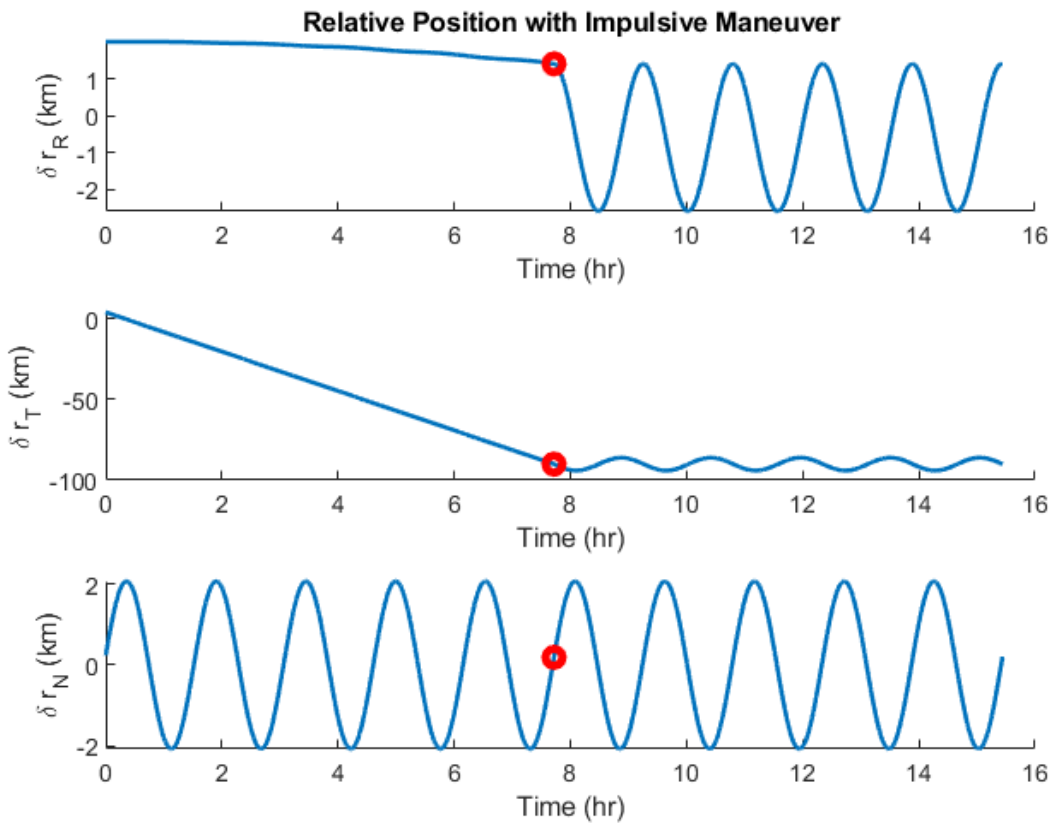


Figure 16: Location of Impulse and Corresponding Relative Position

## 5 Linear Relative Motion

### 5.1 Initial Conditions

The initial conditions for this linearized simulation are identical to the conditions used in the previous section.

Chief:

$$a = 6782.42 \text{ km}$$

$$e = 0.0002.42$$

$$i = 51.6438^\circ$$

$$\Omega = 331.1221^\circ$$

$$\omega = 355.8915^\circ$$

$$M_0 = 76.9789^\circ$$

From the Chief orbit, small variations were applied to the Keplerian orbital elements to produce a Deputy orbit with a  $1^\circ$  change in inclination,  $\Omega$ , and  $\omega$ .

Deputy:

$$\begin{aligned}a &= 6782.42 \text{ km} \\e &= 0.0002.42 \\i &= 52.6438^\circ \\ \Omega &= 332.1221^\circ \\ \omega &= 356.8915^\circ \\ M_0 &= 76.9789^\circ\end{aligned}$$

These changes in orbital elements are a valid set of initial conditions due to the relation of relative position to the value of  $r_0$ , satisfying:

$$\|\vec{\rho}\| \leq 0.001 \|r_0\|$$

By treating these initial Keplerian elements as osculating quantities, computing the corresponding initial position and velocity in the appropriate inertial frame (Earth- Centered Inertial for an Earth-orbiting mission), leads to the following vectors:

Chief:

$$\begin{aligned}r_0^{ECI} &= [6730.078, 841.009, 2.5023]' [\text{km}] \\v_0^{ECI} &= [-0.951, 7.606, 0.121]' [\text{km/s}]\end{aligned}$$

Deputy:

$$\begin{aligned}r_0^{ECI} &= [6729.822, 843.058, 2.5508]' [\text{km}] \\v_0^{ECI} &= [-0.953, 7.601, 0.123]' [\text{km/s}]\end{aligned}$$

From the ECI vectors, relative position and velocity (taken and expressed in the chief RTN frame) can be propagated as such:

Relative Position and Velocity:

$$\begin{aligned}r_0^{RTN} &= [-3.146 \cdot 10^{-4}, 2.066, 0.016]' [\text{km}] \\v_0^{RTN} &= [-5.388 \cdot 10^{-9}, -3.557 \cdot 10^{-7}, 0.002]' [\text{km/s}]\end{aligned}$$

## 5.2 Rectilinear HCW Propagation

### 5.2.1 Integration Constants

The analytical solution to the HCW equations can be expressed as follows:

$$\begin{aligned}x(t) &= c_1 + c_2 \sin(nt) + c_3 \cos(nt) \\y(t) &= c_4 - 1.5nc_1t + 2c_3 \sin(nt) + 2c_2 \cos(nt) \\z(t) &= c_5 \sin(nt) + c_6 \cos(nt)\end{aligned}$$

The integration constants of the HCW equations can be expressed from the initial conditions as follows:

$$\begin{aligned}
 c_1 &= 4x(0) + \frac{2\dot{y}(0)}{n} = -6.2944e-04 \text{ km} \\
 c_2 &= \frac{\dot{x}(0)}{n} = -1.0722e-14 \text{ km} \\
 c_3 &= -3x(0) - \frac{2\dot{y}(0)}{n} = 6.2944e-04 \text{ km} \\
 c_4 &= y(0) - \frac{2\dot{x}(0)}{n} = 2.0658 \text{ km} \\
 c_5 &= \frac{\dot{z}(0)}{n} = 2.0662 \text{ km} \\
 c_6 &= z(0) = 0.0160 \text{ km}
 \end{aligned}$$

### 5.2.2 Orbit Propagation

Orbit simulation was propagated from a set of differential equations in rectilinear coordinates known as the Hill-Clohessy-Wiltshire (HCW) equations:

$$\begin{aligned}
 \ddot{x} - 2n\dot{y} - 3n^2x &= 0 \\
 \ddot{y} + 2n\dot{x} &= 0 \\
 \ddot{z} + n^2z &= 0
 \end{aligned}$$

The following plots were produced with a simulation of 15 orbits and an integration step size of 5 seconds.

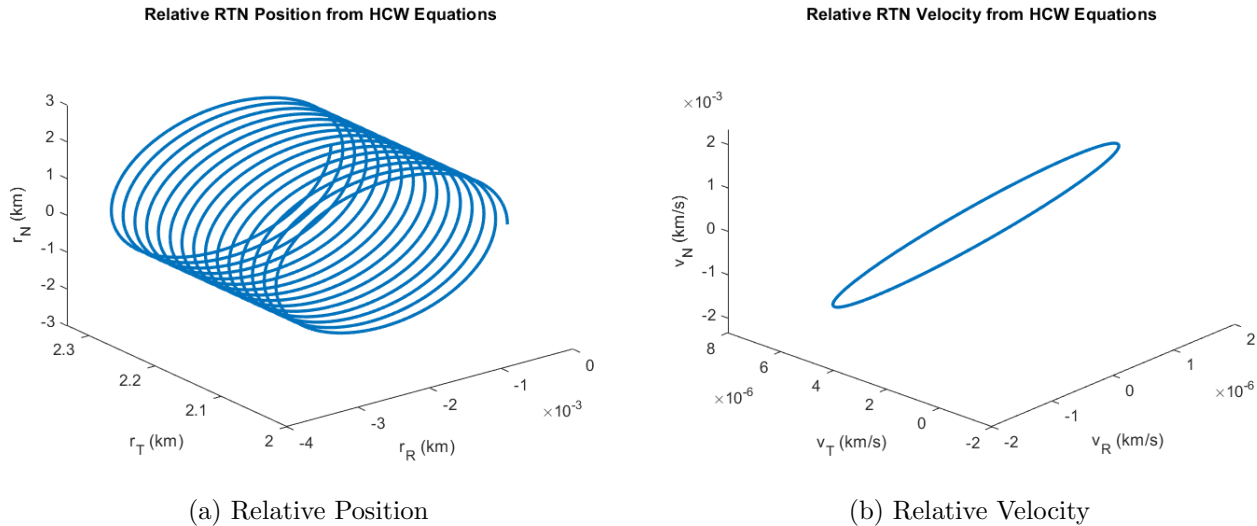


Figure 17: Relative RTN Position and Velocity Vectors

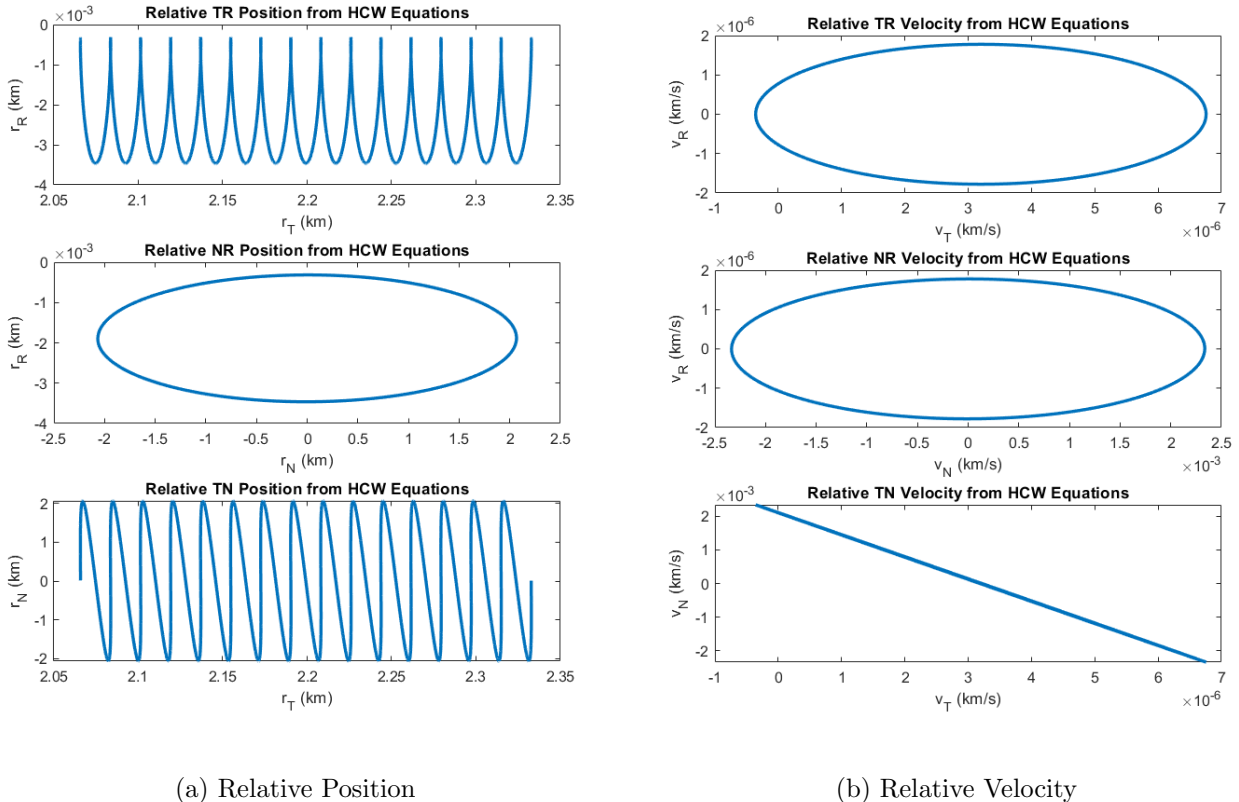


Figure 18: Relative RTN Position and Velocity Vectors

This behavior matches the expectation for this orbit to have a drift since the there exist non-zero time-dependent terms in the linearized equations of relative motion. This is also true despite satisfying the energy matching condition since the time dependence no longer bounds periodic motion.

### 5.3 Curvilinear HCW Propagation

#### 5.3.1 Integration Constants

The HCW equations in curvilinear coordinates have the exact same solution as those for rectilinear coordinates, and so a calculation of the curvilinear integration constants is a simple substitution given by:  $(x, y, z) \rightarrow (\delta r, a\theta_r, a\phi_r)$ . Now the rectilinear integration constants can be calculated:

$$\begin{aligned}
 c_1 &= 4\delta r(0) + \frac{2a\dot{\theta}_r(0)}{n} = -0.0019 \text{ km} \\
 c_2 &= \frac{\delta\dot{r}(0)}{n} = -4.7675e-06 \text{ km} \\
 c_3 &= 3\delta r(0) + \frac{2a\dot{\phi}_r(0)}{n} = 0.0016 \text{ km} \\
 c_4 &= a\theta_r(0) - \frac{2\delta\dot{r}(0)}{n} = 2.0658 \text{ km}
 \end{aligned}$$

$$c_5 = \frac{a\dot{\phi}_r(0)}{n} = 2.0662 \text{ km}$$

$$c_6 = a\phi_r(0) = 0.0160 \text{ km}$$

### 5.3.2 Orbit Propagation

In curvilinear coordinates, the HCW equations take the following form:

$$\begin{aligned}\delta\ddot{r} - 2a_0 n_0 \dot{\theta}_r - 3n_0^2 \delta r &= 0 \\ a_0 \ddot{\theta}_r - 2n_0 \delta \dot{r} &= 0 \\ \ddot{\phi}_r + n_0^2 \phi_r &= 0\end{aligned}$$

The following plots were produced with a simulation of 15 orbits and an integration step size of 5 seconds.

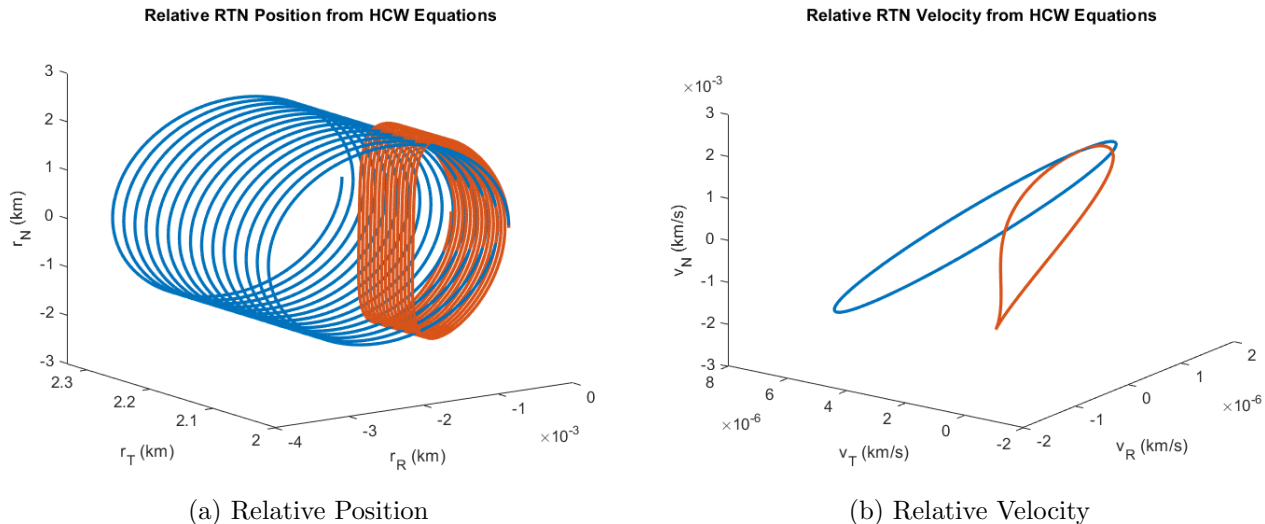


Figure 19: Relative RTN Position and Velocity Vectors

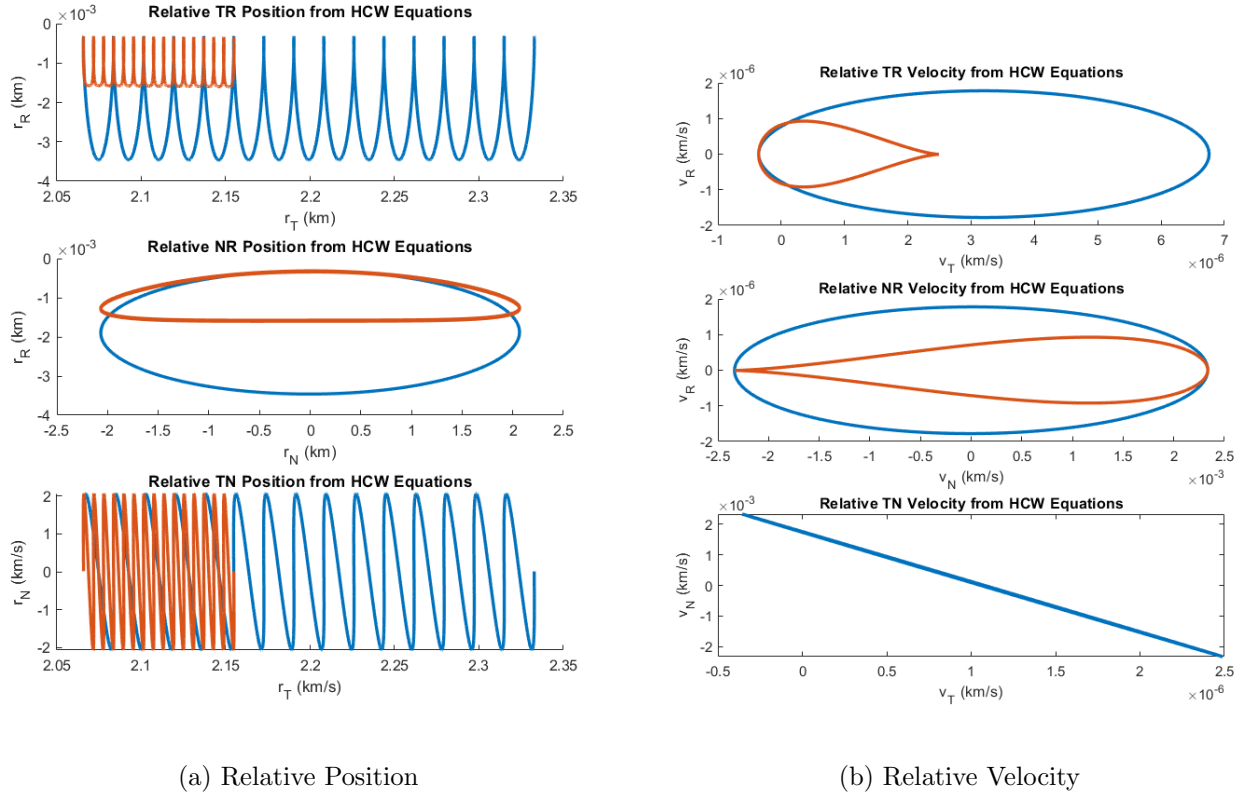


Figure 20: Relative RTN Position and Velocity Vectors

A curvilinear transformation on the equations of relative motion relaxes the linearization of the orbit, and reduces the along-track drift error in the linearized propagation. Therefore, we expect the resulting orbit to have a smaller periodic drift as seen in on the superimposed plots.

## 6 Linearized Equations of Relative Motion for Eccentric Orbits

This section further explores the analysis of relative spacecraft motion according to the Tschauner-Hempel (TH) equations. These equations relate to both a Cartesian relative state and orbit element differences. Mathematical analyses and simulated results are shown in this section.

## 6.1 Yamanaka-Andersen (YA) and Schaub Integration Constant Differences

The Yamanaka-Andersen solution to the Tschauner-Hempel equations are provided in the subsequent equations (taken from Alfriend eq. 5.124):

$$\begin{aligned}\bar{x}(f) &= c_1 k \sin(f) + c_2 k \cos(f) + c_3 [2 - 3ekI \sin(f)] \\ \bar{y}(f) &= c_4 + c_1 k \left(1 + \frac{1}{k}\right) \cos(f) - c_2 k \left(1 + \frac{1}{k}\right) \sin(f) - 3c_3 k^2 I \\ \bar{z}(f) &= c_5 \cos(f) + c_6 \sin(f)\end{aligned}$$

Where  $k = 1 + e \cos(f)$  and  $I = \int_{f_0}^f [1 + e \cos(f)]^{-2} df$ .

The linear mapping between the Cartesian relative state and Schaub's orbital element differences is provided in the following equations (taken from Schaub eq. 14.117):

$$\begin{aligned}\bar{x}(f) &= \frac{\delta a}{a} + k \frac{e \delta M}{\eta^3} \sin(f) - \frac{k \delta e}{\eta^2} \cos(f) \\ \bar{y}(f) &= k^2 \frac{\delta M}{\eta^3} + \delta \omega + (2 + e \cos(f)) \frac{\delta e}{\eta^2} \sin(f) + \cos(i) \delta \Omega \\ \bar{z}(f) &= \sin(f + \omega) \delta i - \cos(f + \omega) \sin(i) \delta \Omega\end{aligned}$$

Where  $k = 1 + e \cos(f)$  and  $\eta = \sqrt{1 - e^2}$ .

From these two sets of expressions, by liking similar terms, the following relationships have been derived:

$$c_1 \approx e \left( \frac{\delta M}{\eta^3} + \frac{3\delta a I}{2a} \right)$$

$$c_2 \approx -\frac{\delta e}{\eta^2}$$

$$c_3 \approx \frac{\delta a}{2a}$$

$$c_4 \approx k^2 \left( \frac{3\delta a}{2a} I + \frac{\delta M}{\eta^3} \right) + \delta \omega + \cos(i) \delta \Omega$$

$$c_5 \approx \delta i \sin(\omega) - \sin(i) \delta \Omega \cos(\omega)$$

$$c_6 \approx \delta i \cos(\omega) + \sin(i) \delta \Omega \sin(\omega)$$

## 6.2 YA and Schaub Relative Velocity Expressions

From the position expressions, subsequent velocity expressions can be derived for both the YA and Schaub solutions.

For the derivation of the YA velocity vector:

$$\begin{aligned}\dot{x}(f) &= (c_1 k - 3e k I c_3) \cos(f) - \left(\frac{3e}{k} + c_2 k\right) \sin(f) - c_2 e \sin(f) \cos(f) + (3e^2 I c_3 - c_1 e) \sin^2(f) \\ \dot{y}(f) &= (6c_3 k e I - c_1 k - c_1) \sin(f) - (c_2 k + c_2) \cos(f) + c_2 e \sin^2(f) - c_1 e \cos(f) \sin(f) - 3c_3 \\ \dot{z}(f) &= c_6 \cos(f) - c_5 \sin(f)\end{aligned}$$

and for the derivation of the Schaub velocity vector:

$$\begin{aligned}\dot{x}(f) &= \frac{ke\delta M}{\eta^3} \cos(f) + \left(\frac{ke}{\eta^3} \frac{n_d - n_c}{\dot{f}} + \frac{k\delta e}{\eta^2}\right) \sin(f) - \frac{e\delta e}{\eta^2} \sin(f) \cos(f) - e^2 \frac{\delta M}{\eta^3} \sin^2(f) \\ \dot{y}(f) &= -2ke \frac{\delta M}{\eta^3} \sin(f) + \frac{2\delta e}{\eta^2} \cos(f) + \frac{e\delta e}{\eta^2} (\cos^2(f) - \sin^2(f)) + \frac{k^2}{\eta^3} \frac{n_d - n_c}{\dot{f}} \\ \dot{z}(f) &= (\cos(\omega)\delta i + \sin(\omega)\sin(i)\delta\Omega) \cos(f) + (\cos(\omega)\sin(i)\delta\Omega - \sin(\omega)\delta i) \sin(f)\end{aligned}$$

where  $\dot{f} = \sqrt{\frac{\mu}{a^3(1-e^2)^3}} [1 + e \cos(f)]^2$ .

## 7 Eccentric Orbit Simulation Analysis

### 7.1 Initial Conditions

As seen in the following table, the initial conditions for this analysis have been derived from the previous set of initial conditions as described in this report. For the first case, eccentricity was set to be 0.15 to invoke eccentric linearization, and the only changes to the deputy orbit are in inclination (-0.001°), and argument of perigee (0.001°), and true anomaly (0.001°):

Table 3: Initial Conditions

	Case 1: $e \geq 0.1$		Case 2: $\delta a$		Case 3: $e \geq 0.5$	
	Chief	Deputy	Chief	Deputy	Chief	Deputy
a (km)	6782.423	6782.423	6782.423	6783.423	6782.423	6783.423
e	0.15	0.15	0.10	0.10	0.70	0.70
i (deg)	51.6438	51.6428	51.6438	51.6428	51.6438	51.6428
$\Omega$ (deg)	331.1221	331.1221	331.1221	331.1221	331.1221	331.1221
$\omega$ (deg)	355.8915	355.8925	355.8915	355.8925	355.8915	355.8925
f (deg)	0.000	0.001	0.000	0.001	0.000	0.001

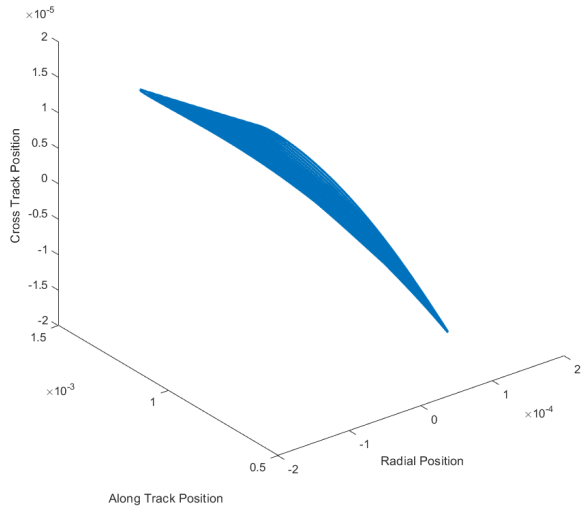
### 7.2 Yamanaka-Andersen (YA) Solution

Based on the initial conditions for Case 1 and the analytical solution presented in the prior section, the following integration constants were calculated for the YA solution:

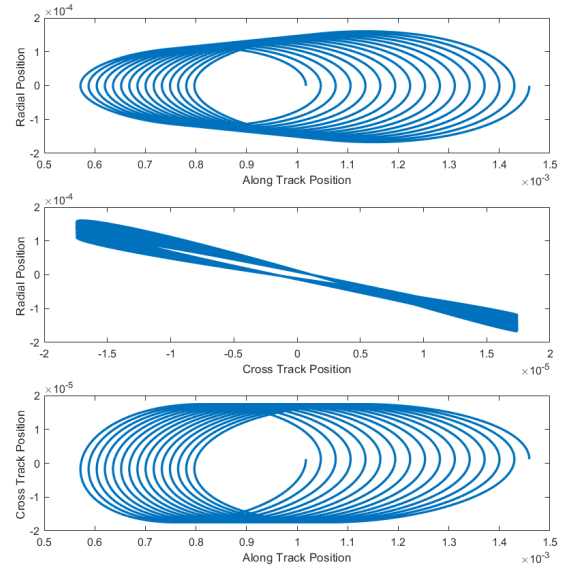
Table 4: YA Integration Constants

$$\begin{aligned}
 c_1 &= 1.1342e-04 \\
 c_2 &= 1.5917e-06 \\
 c_3 &= -1.1414e-06 \\
 c_4 &= 7.7360e-04 \\
 c_5 &= 1.2327e-06 \\
 c_6 &= -1.7410e-05
 \end{aligned}$$

From these initial conditions, the relative position and velocity was propagated over 15 orbits using true anomaly as the independent variable. The following plots represent the relative position and velocity in 3D and in the TR, NR, and TN planes:



(a) 3D YA Position Solution



(b) RTN-Plane YA Position Solution

Figure 21: YA Position Solution

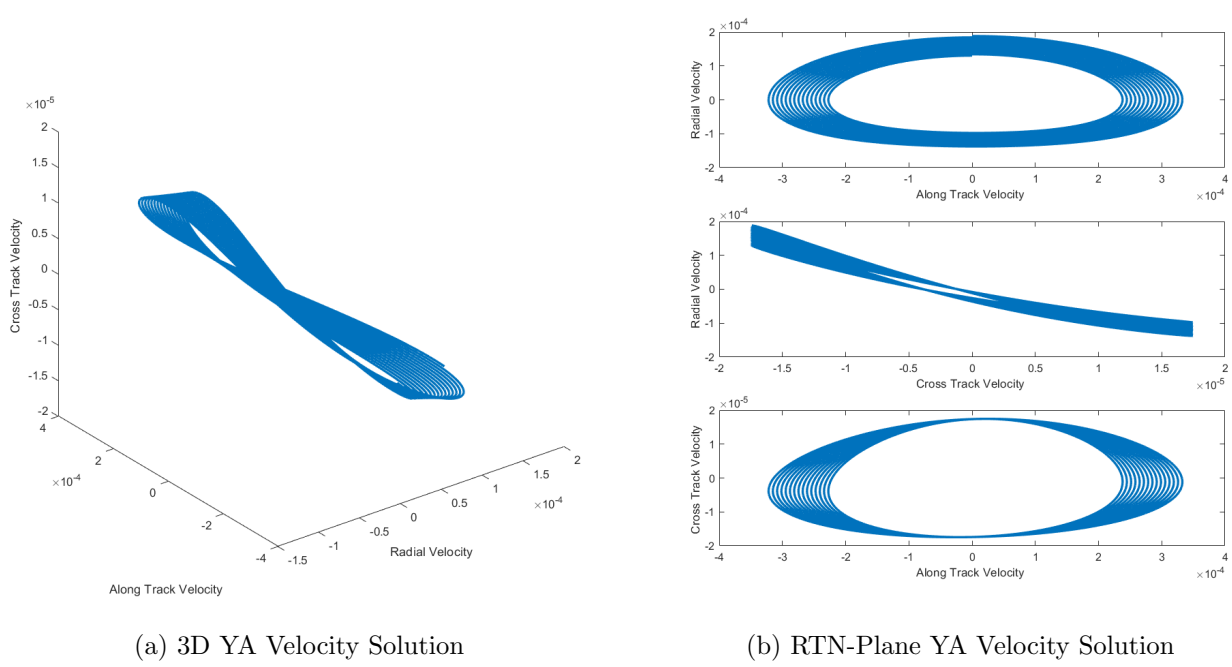


Figure 22: YA Velocity Solution

Given the initial conditions and integration constants, we expect to see drift in the along-track and radial direction since there are non-zero integration constants which are applied to the integration upon true anomaly. Despite meeting the energy-matching criteria of a zero relative semi-major axis, these non-zero coefficients create drift in the propagation, and unbound the relative motion.

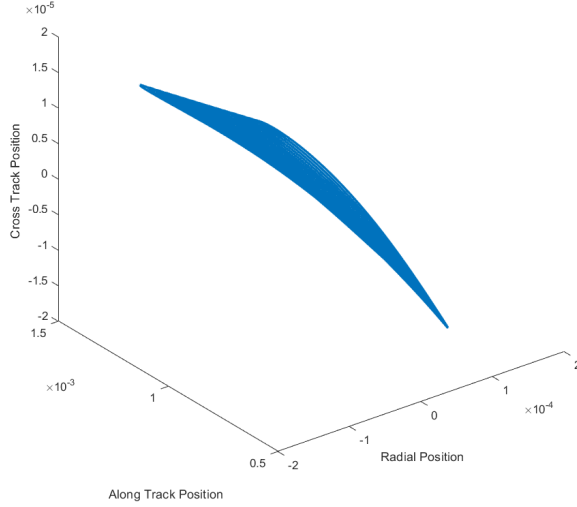
### 7.3 Schaub Solution

Continuing with the initial conditions for Case 1, the orbital element differences for the Schaub solution were computed as follows:

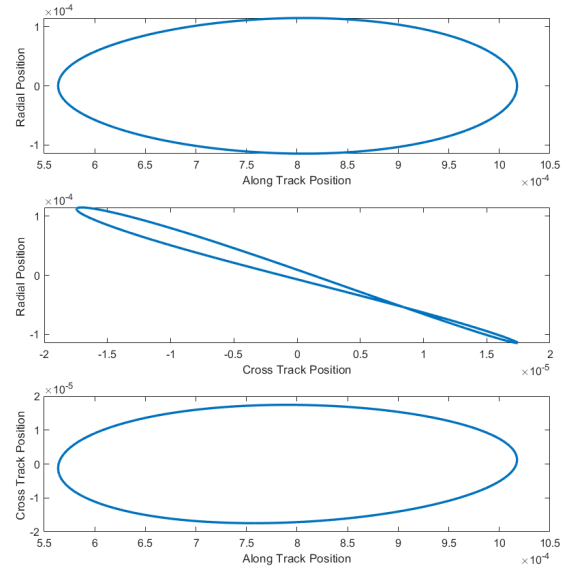
Table 5: Schaub Orbital Element Differences

$$\begin{aligned}
 \delta a &= 0.0000 \\
 \delta e &= -2.2846e-11 \\
 \delta i &= -1.7453e-05 \\
 \delta \Omega &= 0.0000 \\
 \delta \omega &= 1.7453e-05 \\
 \delta M_0 &= 7.3077e-04
 \end{aligned}$$

Like the YA solutions, the relative position and velocity was propagated over 15 orbits using true anomaly as the independent variable. The following plots represent the relative position and velocity in 3D and in the TR, NR, and TN planes:

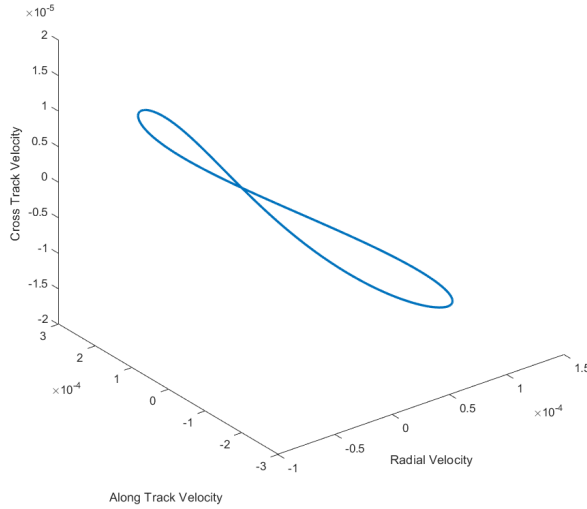


(a) 3D YA Position Solution

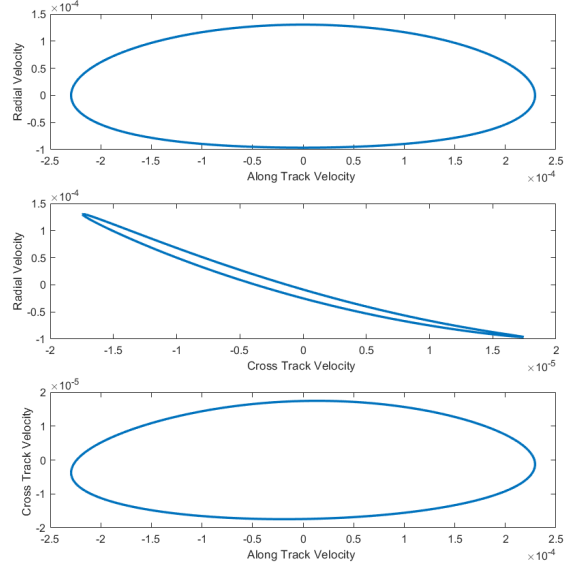


(b) RTN-Plane Schaub Position Solution

Figure 23: Schaub Position Solution



(a) 3D Schaub Velocity Solution



(b) RTN-Plane Schaub Velocity Solution

Figure 24: Schaub Velocity Solution

Unlike the YA propagation, the presence of zero-value orbital element differences means that we do not experience drift in any noticeable direction.

## 7.4 Numerical Solution

By comparing the true relative position and velocity from numerical propagation to these results, the following plots were produced, representing the superimposed relative position and velocity of all three methods in 3D and in the RTN planes, as well as difference error between the YA and Schaub solutions from the true state reference:

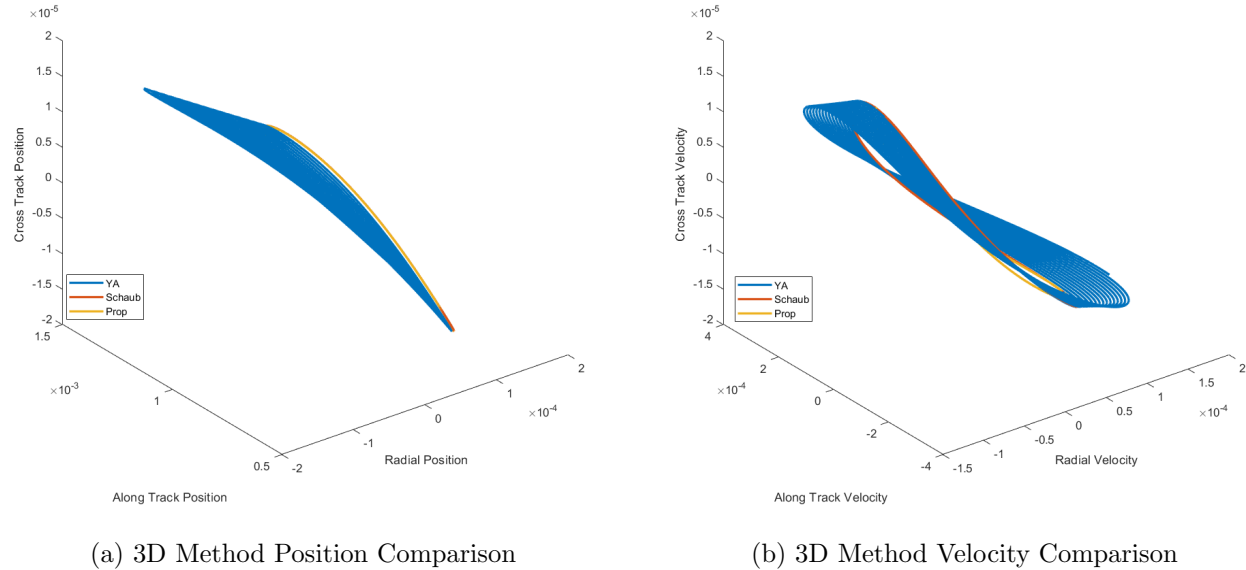
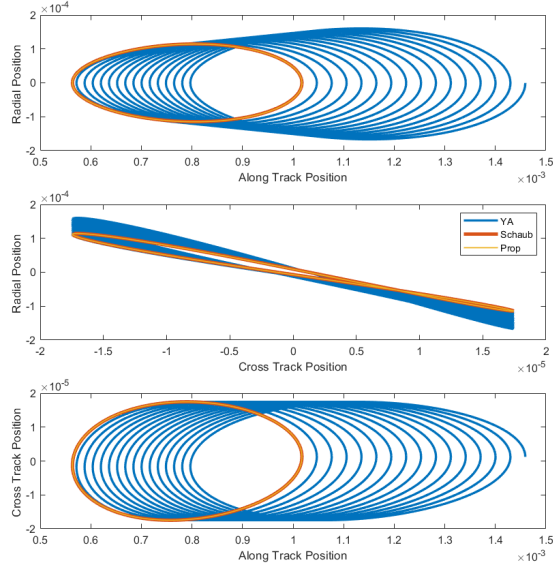
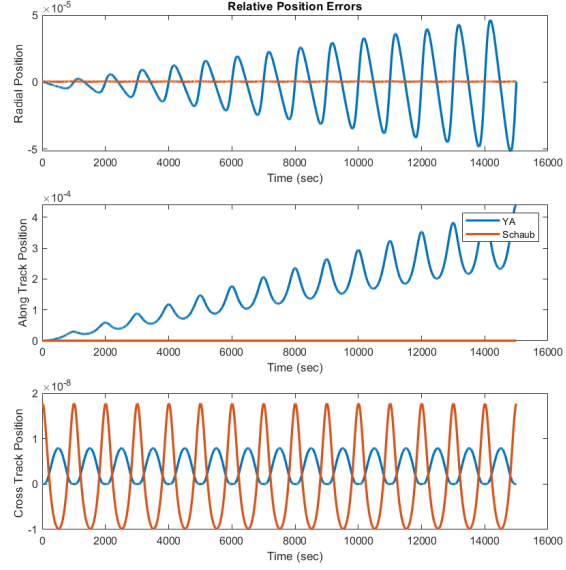


Figure 25: 3D Method Comparison

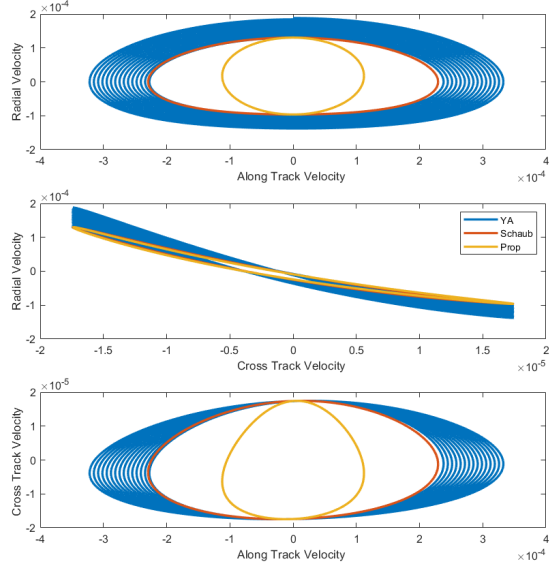


(a) RTN-Plane Method Position Comparison

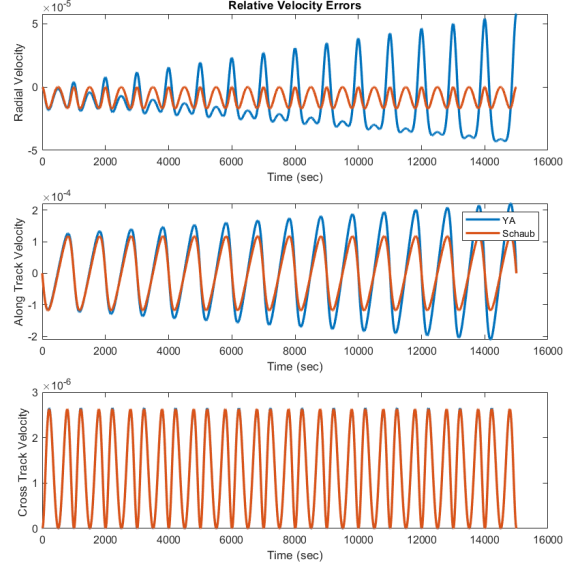


(b) RTN-Plane Method Position Error

Figure 26: RTN-Plane Method Position Comparison



(a) RTN-Plane Method Velocity Comparison



(b) RTN-Plane Method Velocity Error

Figure 27: RTN-Plane Method Velocity Comparison

From these plots (primarily the error plots), it is clear to see that the Schaub solution was a more accurate representation due to the considerations of energy-matching criteria in the numerical integration. By eliminating the interference of radial and along track drift, the Schaub solution matches much closer to the true state in both position and velocity than the YA solution.

## 7.5 Non-zero $\delta a$ Results

Now utilizing the initial conditions for Case 2 in Table 3, we have induced a difference in semi-major axis and violated the energy-matching condition. The integration constants and orbital element differences for the YA and Schaub solutions, respectively, are as follows:

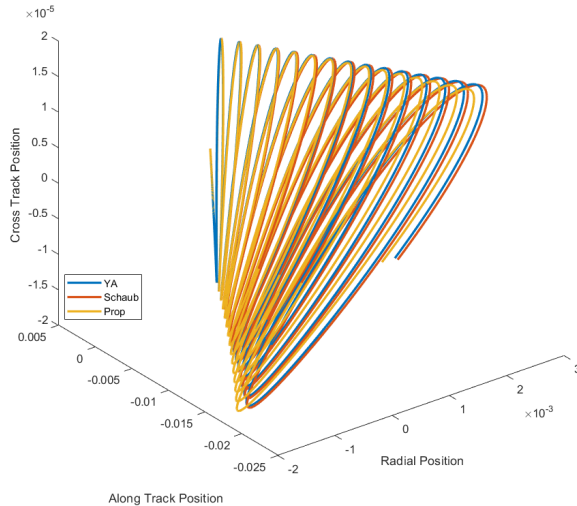
Table 6: YA Integration Constants

$$\begin{aligned} c_1 &= 8.2843e-05 \\ c_2 &= 1.5525e-06 \\ c_3 &= 7.2630e-05 \\ c_4 &= 8.4363e-04 \\ c_5 &= 1.2329e-06 \\ c_6 &= -1.7408e-05 \end{aligned}$$

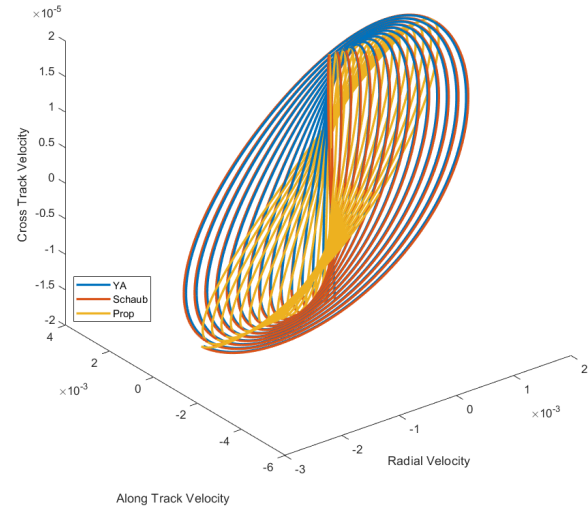
Table 7: Schaub Orbital Element Differences

$$\begin{aligned} \delta a &= 1.0000 \\ \delta e &= -1.5231e-11 \\ \delta i &= -1.7453e-05 \\ \delta \Omega &= 0.0000 \\ \delta \omega &= 1.7453e-05 \\ \delta M_0 &= 8.1408e-04 \end{aligned}$$

From these conditions, the relative position and velocity was propagated over 15 orbits using true anomaly as the independent variable. The following plots represent the relative position and velocity in 3D and in the TR, NR, and TN planes, as well as error between the two methods as compared to the true relative state:

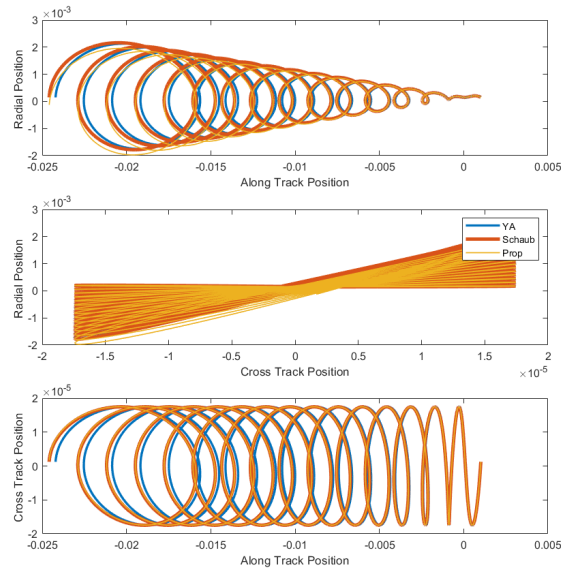


(a) 3D Method Position Comparison

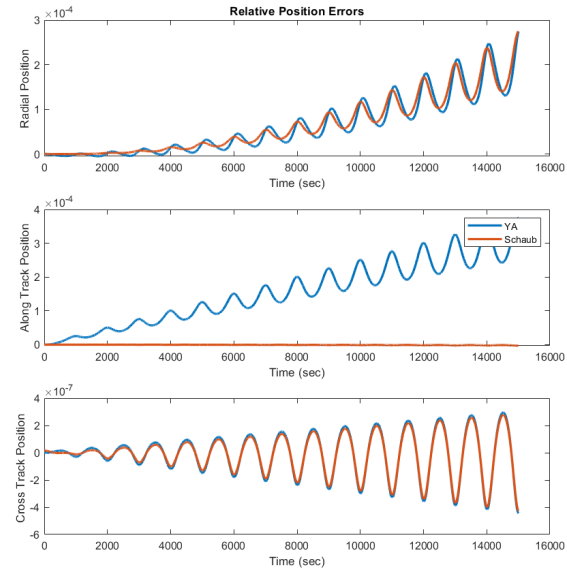


(b) 3D Method Velocity Comparison

Figure 28: 3D Method Comparison



(a) RTN-Plane Method Position Comparison [km]



(b) RTN-Plane Method Position Error [km]

Figure 29: RTN-Plane Method Position Comparison

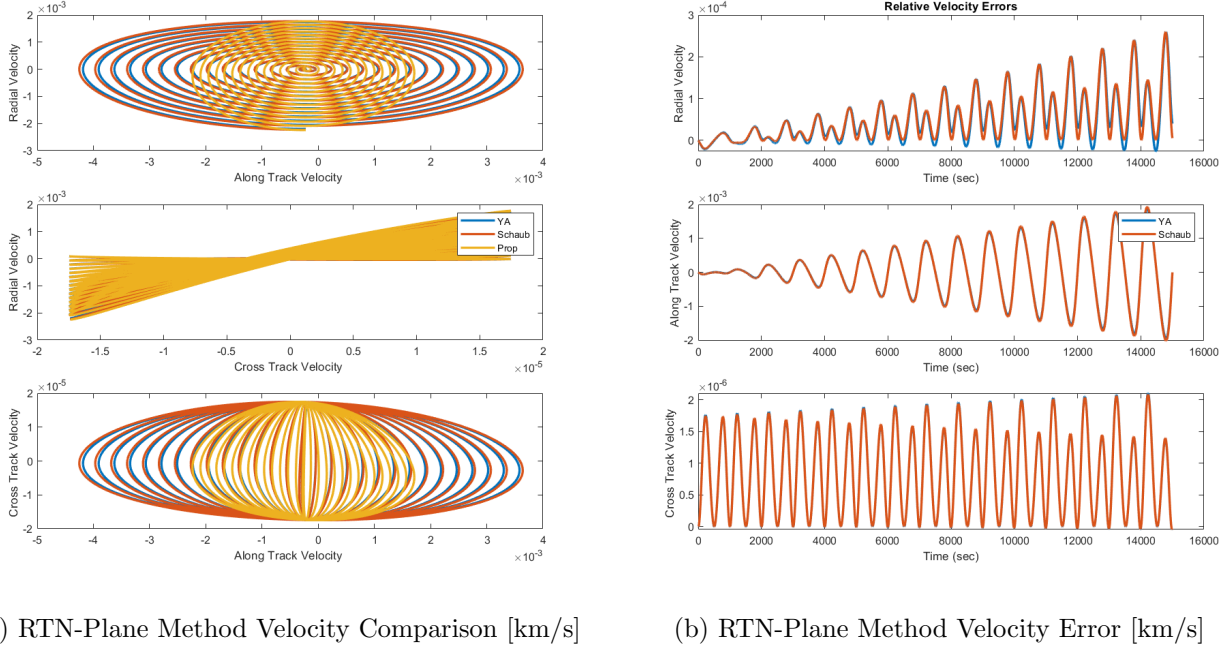


Figure 30: RTN-Plane Method Velocity Comparison

Unlike the first case where the Schaub solution provided a much closer match to the true states than the YA, the inclusion of a difference in semi-major axis unbounds the relative motion for all cases, and the YA and Schaub solutions become very similar. The only advantage Schaub has in this scenario is when considering along track drift of the position vector.

## 7.6 Highly-Eccentric Results

Now utilizing the initial conditions for Case 3 in Table 3, we have kept the difference in semi-major axis from the previous section and increased the chief and deputy eccentricity to 0.7 to represent highly-elliptical orbits. The integration constants and orbital element differences for the YA and Schaub solutions, respectively, are as follows:

Table 8: YA Integration Constants

$$\begin{aligned}
 c_1 &= 2.4233e-04 \\
 c_2 &= 3.0160e-06 \\
 c_3 &= 7.100e-05 \\
 c_4 &= 3.6331e-04 \\
 c_5 &= 1.2329e-06 \\
 c_6 &= -1.7408e-05
 \end{aligned}$$

Table 9: Schaub Orbital Element Differences

$$\begin{aligned}
 \delta a &= 1.0000 \\
 \delta e &= -1.0662e-10 \\
 \delta i &= -1.7453e-05 \\
 \delta \Omega &= 0.0000 \\
 \delta \omega &= 1.7453e-05 \\
 \delta M_0 &= 1.2603e-04
 \end{aligned}$$

From these conditions, the relative position and velocity was propagated over 15 orbits using true anomaly as the independent variable. The following plots represent the relative position and velocity in 3D and in the TR, NR, and TN planes, as well as error between the two methods as compared to the true relative state:

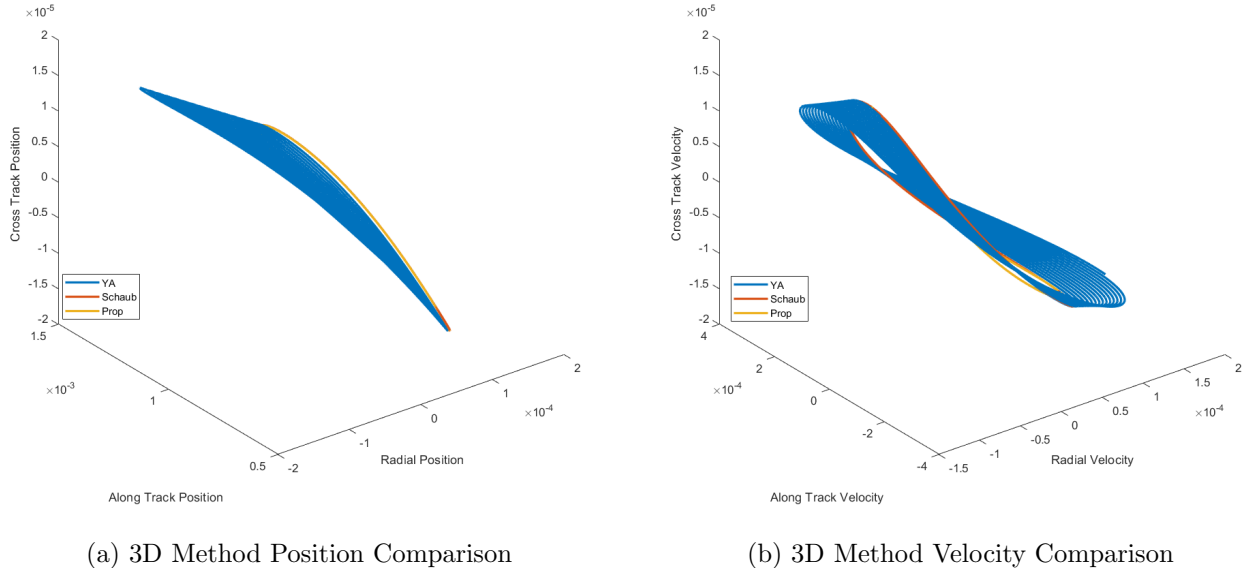
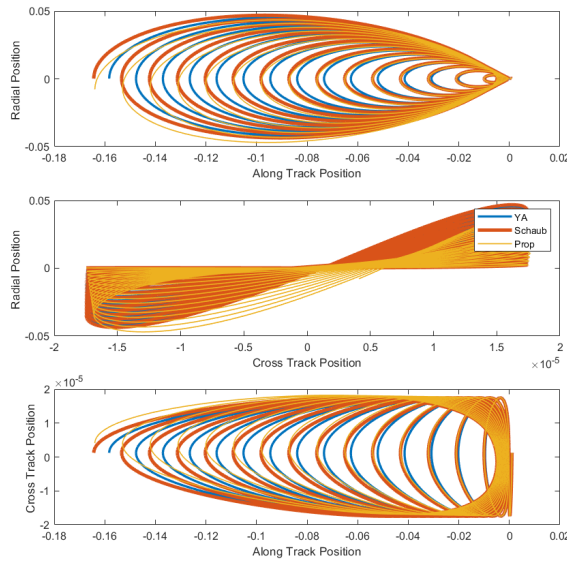
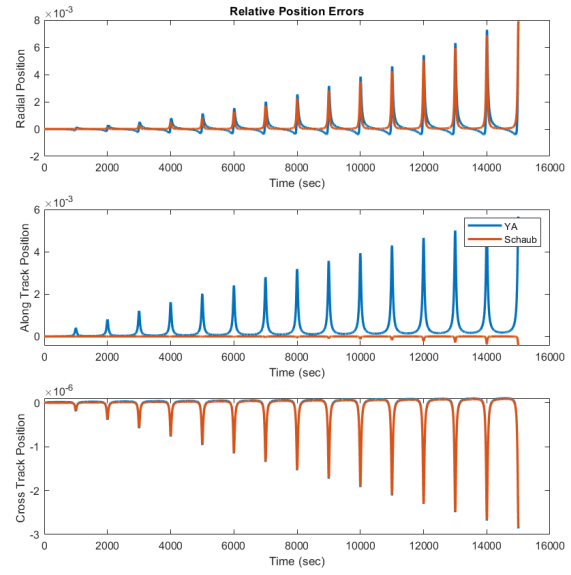


Figure 31: 3D Method Comparison

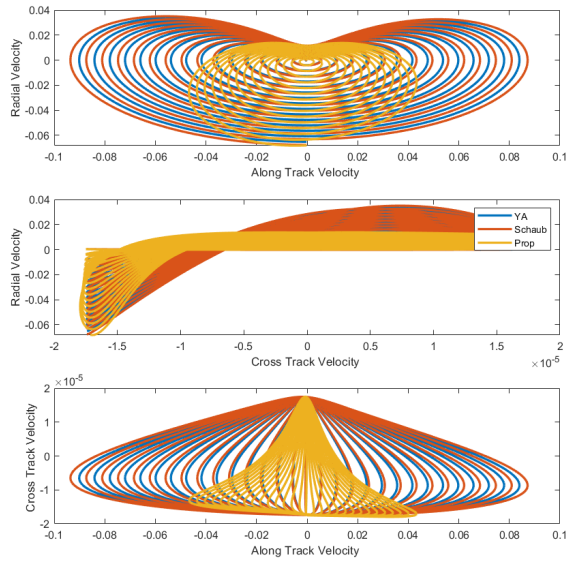


(a) RTN-Plane Method Position Comparison

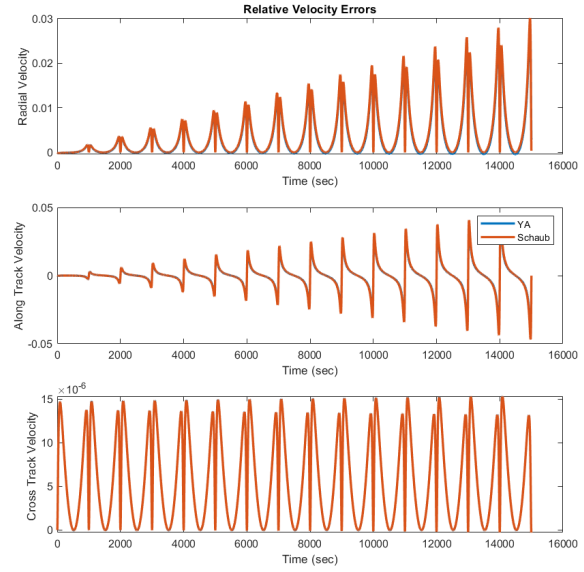


(b) RTN-Plane Method Position Error

Figure 32: RTN-Plane Method Position Comparison



(a) RTN-Plane Method Velocity Comparison



(b) RTN-Plane Method Velocity Error

Figure 33: RTN-Plane Method Velocity Comparison

For the highly-elliptic case, the Schaub solution outperforms the YA solution in along track drift error correction again, and the other terms are relatively equal. It is important to note, however, that relative semi-major axis change was still non-zero for this case as it was in the last one. For identical semi-major axes, the error would follow the same behavior of that of case one, but with a higher order of magnitude

of error in the YA solution results.

## 8 Perturbed $J_2$ Relative Orbit Motion in Near-Circular Orbits

### 8.1 Initial Conditions

For this simulation, the osculating initial conditions for the absolute (chief) states were selected to be the initial conditions of Problem Set 3 (see below):

Chief:

$$\begin{aligned}a &= 6782.42 \text{ km} \\e &= 0.0002.42 \\i &= 51.6438^\circ \\\Omega &= 331.1221^\circ \\\omega &= 355.8915^\circ \\f &= 77.0002^\circ\end{aligned}$$

These initial conditions are a valid set of parameters for a near-circular assumption since  $e \ll 1$ .

For the initial state of the deputy orbit, the following osculating quasi-non-singular relative orbit elements were prescribed:

$$a_c(\delta a, \delta\lambda, \delta e_x, \delta e_y, \delta i_x, \delta i_y) = (0, 100, 50, 100, 30, 200) \text{ m}$$

From these relative orbital elements, the initial Keplerian orbital elements of the deputy can be calculated as:

Deputy:

$$\begin{aligned}a &= 6782.42 \text{ km} \\e &= 0.0002.42 \\i &= 51.6438^\circ \\\Omega &= 331.1221^\circ \\\omega &= 0.3180^\circ \\f &= 72.5740^\circ\end{aligned}$$

### 8.2 Osculating Quasi-Non-Singular Orbital Elements

With these initial conditions, a numerical integration of the equations of motion for the chief and the deputy orbits using position and velocity as state variables was performed over 20 orbits with a time increment of 5 seconds. The RK4 solver was selected for all numerical integration completed in Simulink.

This propagation was conducted over the prescribed initial conditions with and without  $J_2$  effects. The following plots represent the results of the simulation:

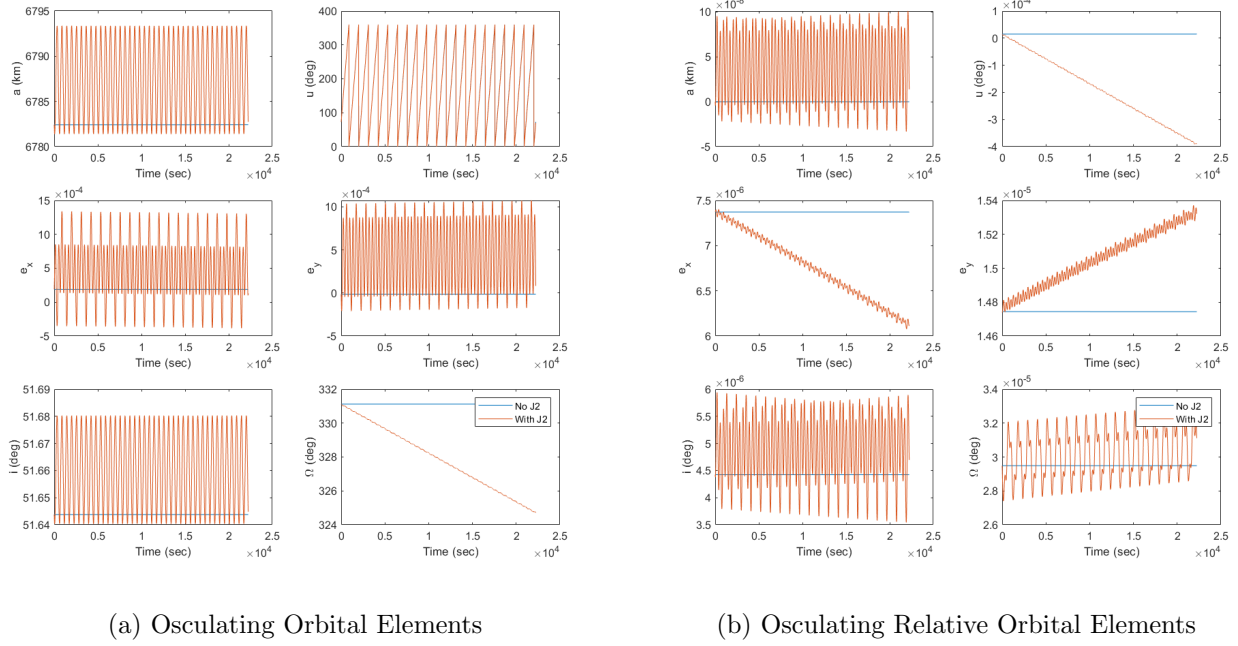


Figure 34: Osculating Quasi-Non-Singular OE and ROE

### 8.3 Mean Quasi-Non-Singular Orbital Elements

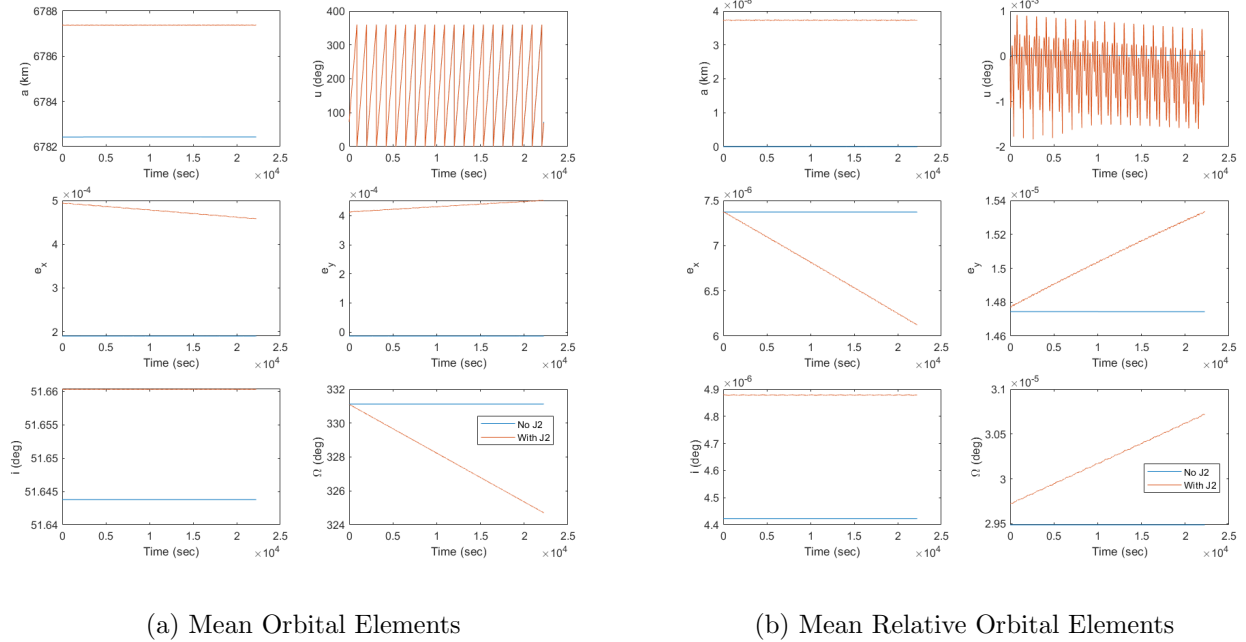
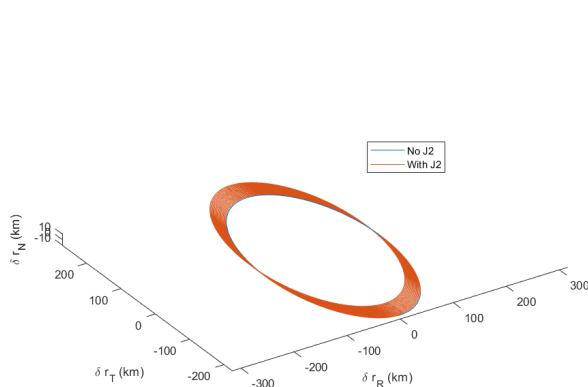
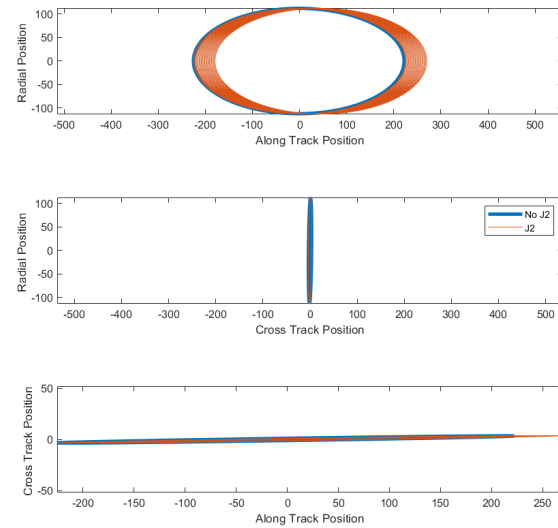


Figure 35: Mean Quasi-Non-Singular OE and ROE

## 8.4 Relative RTN Position



(a) 3D RTN-Plane Method Position Comparison [m]

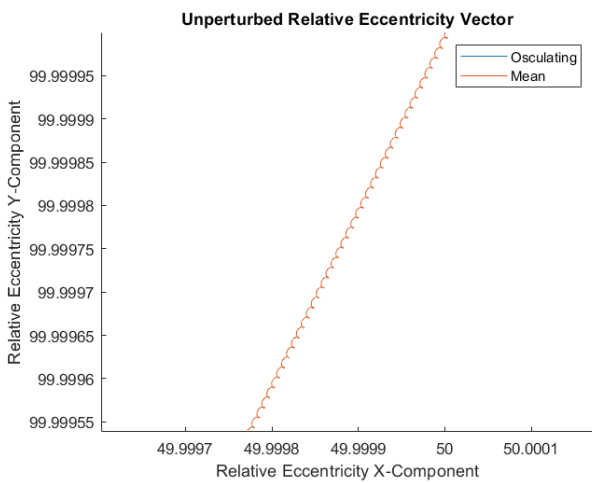


(b) 2D RTN-Plane Method Position Projections [m]

Figure 36: RTN-Plane Method Position Comparison [m]

These results are expected as they represent a standard projection of the RTN position vector into the 2D RTN planes under near-circular orbit.

## 8.5 Relative Quasi-Non-Singular Orbital Elements



(a) Unperturbed Relative Eccentricity Vector

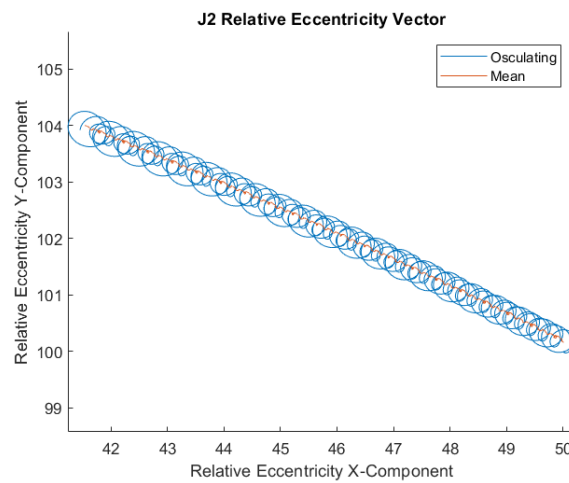
(b) J<sub>2</sub>-Perturbed Relative Eccentricity Vector

Figure 37: Relative Eccentricity Vector Comparison

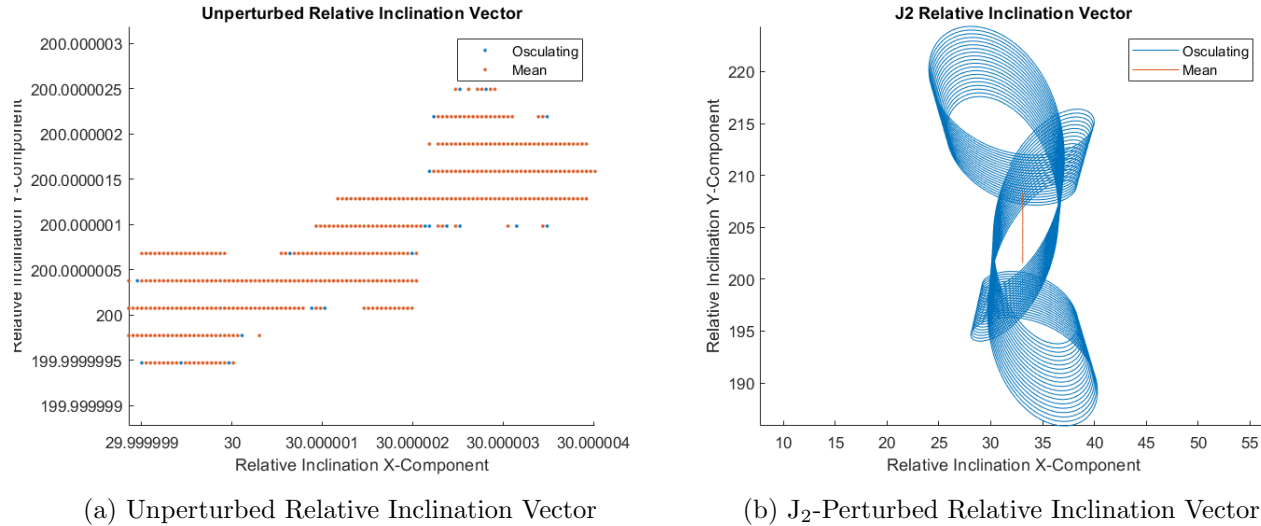


Figure 38: Relative Inclination Vector Comparison

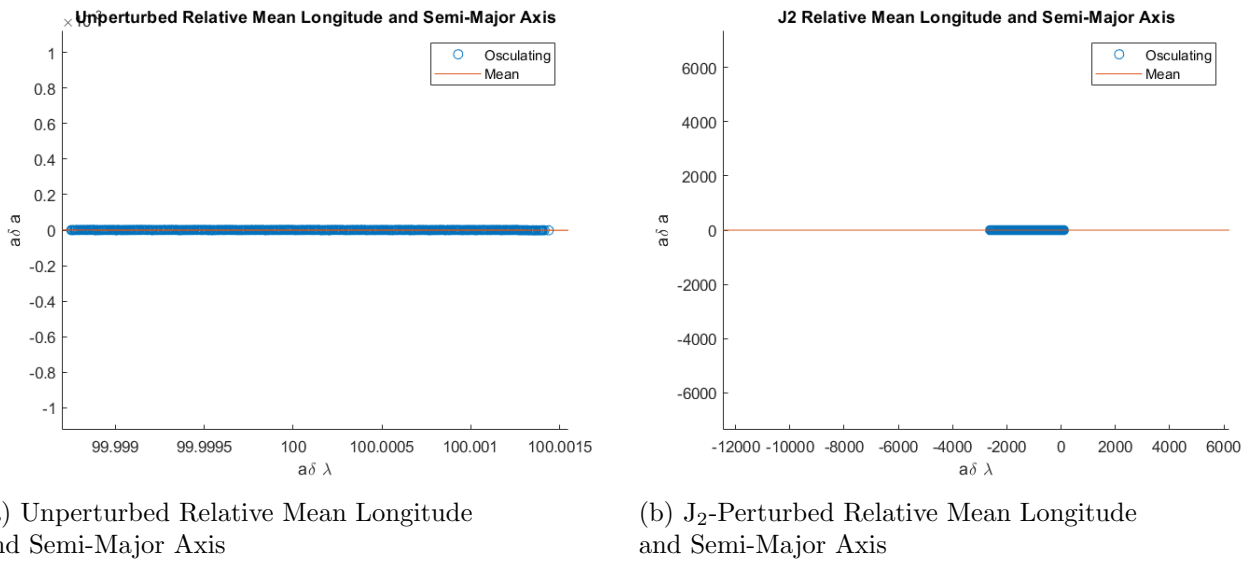


Figure 39: Relative Mean Longitude and Semi-Major Axis Comparison

As it can be seen in the previous set of plots, the J<sub>2</sub> perturbed elements carry both secular and periodic drifts that are not present in the unperturbed dynamics. This is to be expected, as the RTN position vector verified the same expectation.

## 8.6 Minimum Maneuvers

In order to eliminate the J<sub>2</sub> secular effects on the formation, the  $\delta i_x$  term must be set to zero, so the following equation may be used to determine the magnitude and direction of the maneuver:

$$a\delta i_x \approx \delta v_n \cos u_m / n$$

Since  $a\delta i_x$  represents the desired variation of the ROE, in order to make  $\delta i_x = 0$ ,  $a\delta i_x = -30$ :

$$-30 \approx \delta v_n \cos u_m / n$$

In order to minimize  $\delta v_n$ ,  $\cos u_m = 1$ , so  $u_m = 0$ . Simplifying the resulting equation and solving for the maneuver leaves (in the  $v_n$ -direction):

$$\delta v_n \approx -30n \approx -30\sqrt{\frac{\mu}{a_0^3}} \approx -0.0339 \text{ m/s}$$

This change of  $\delta i_x$  provides new initial conditions that should remove  $J_2$  secular effects, with the relative orbital elements set as:

$$a_c(\delta a, \delta\lambda, \delta e_x, \delta e_y, \delta i_x, \delta i_y) = (0, 100, 50, 100, 0, 200) \text{ m}$$

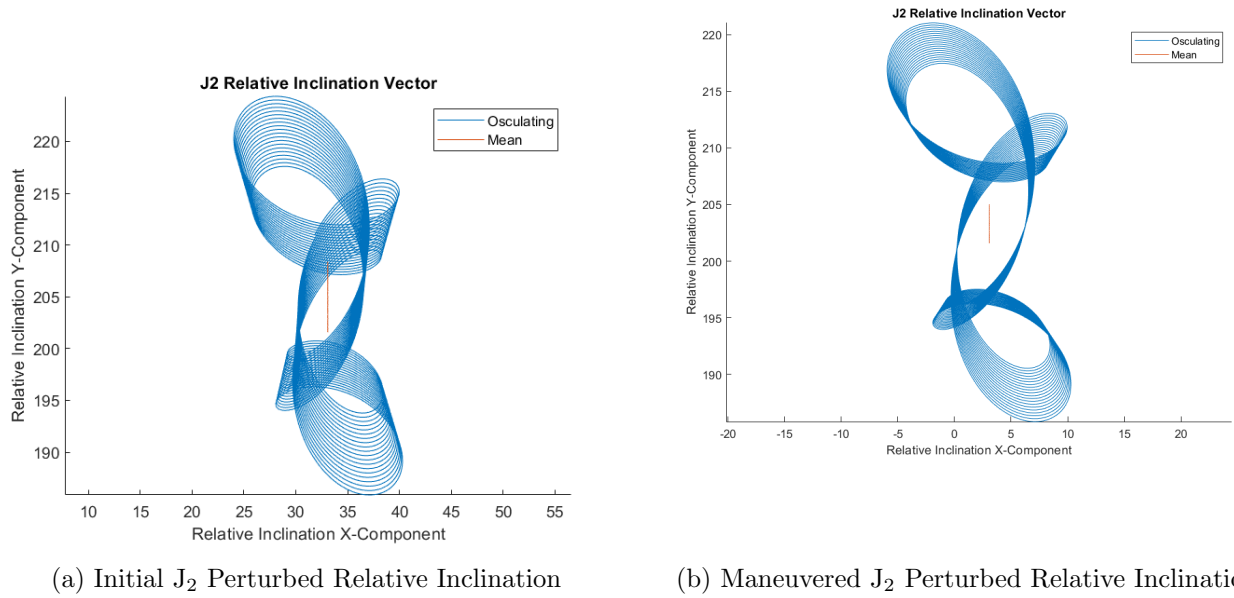
From these relative orbital elements, the initial Keplerian orbital elements of the deputy can be calculated as:

Deputy:

$$\begin{aligned} a &= 6782.42 \text{ km} \\ e &= 0.0002.42 \\ i &= 51.6438^\circ \\ \Omega &= 331.1221^\circ \\ \omega &= 0.3180^\circ \\ f &= 72.5740^\circ \end{aligned}$$

NOTE: These initial conditions are the same as the previous result since the change in ROE terms only varied the Keplerian orbital elements slightly.

By rerunning the simulation with these new conditions, a new reduced-drift plot of the inclination vector may be used to verify the success of the maneuver:

Figure 40: J<sub>2</sub> Perturbed Relative Inclination Comparison

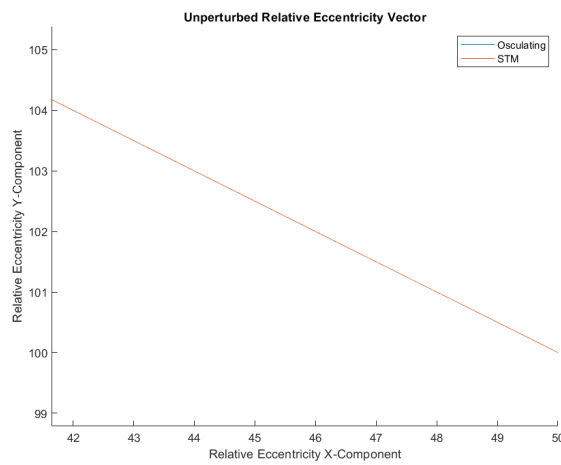
As evidenced by the plot in subfigure (b) in the prior plot, it is clear that there was a reduction in drift within the overall relative inclination vector as expected. The magnitude of the reduction in drift is not as high as expected (to completely eliminate drift), but the reduction of relative inclination drift is a positive indicator that the maneuver was effective in removing the secular effects on the formation.

## 8.7 Secular Evolution of the Relative Orbital Elements

From the state transition matrix based upon the relative orbital elements, it is possible to propagate a set of relative orbital elements by utilizing the following transition matrix:

$$\begin{aligned} \left( \begin{array}{c} \delta\dot{a} \\ \delta\alpha \end{array} \right)_t &= \Phi(t - t_0) \left( \begin{array}{c} \delta\dot{a} \\ \delta\alpha \end{array} \right)_{t_0} \\ \Phi_{F,0} = &\begin{bmatrix} \text{DRAG} & \text{KEPLER} & \text{SECULAR J}_2 \\ \begin{bmatrix} 1 & 0 & 0 & 0 & 0 & 0 \\ (t_F - t_0) & 1 & 0 & 0 & 0 & 0 \\ \frac{\nu}{2}(t_F - t_0)^2 & \nu(t_F - t_0) & 1 & 0 & 0 & \mu(t_F - t_0) \\ 0 & 0 & 0 & 1 & -\dot{\varphi}(t_F - t_0) & 0 \\ 0 & 0 & 0 & \dot{\varphi}(t_F - t_0) & 1 & 0 \\ 0 & 0 & 0 & 0 & 0 & 1 \end{bmatrix} & \end{bmatrix} \\ \nu &= -\frac{3}{2}n \quad \dot{\varphi} = \frac{3}{2}n\gamma(5\cos^2 i - 1) \quad \mu = -\frac{21}{2}n\gamma \sin 2i \quad \lambda = 3n\gamma \sin^2 i \end{aligned}$$

By propagating the relative orbital elements using the state transition matrix, the following comparison plots were produced:



(a) Unperturbed Relative Eccentricity Vector

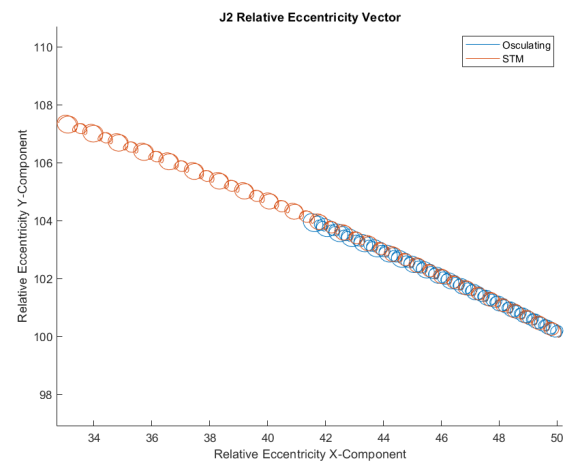
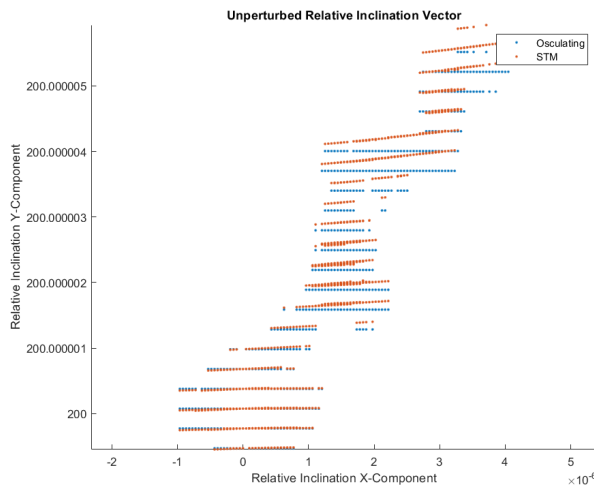
(b) J<sub>2</sub>-Perturbed Relative Eccentricity Vector

Figure 41: Relative Eccentricity Vector Comparison



(a) Unperturbed Relative Inclination Vector

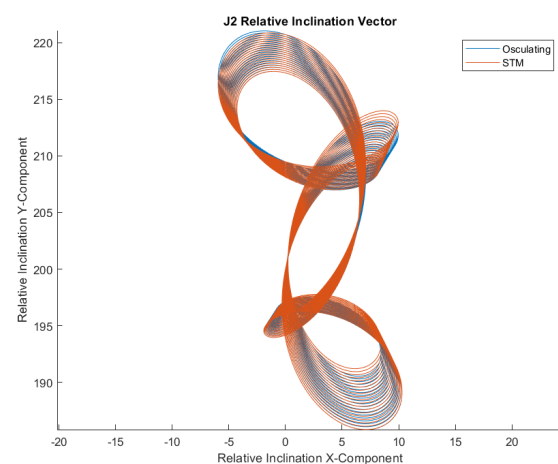
(b) J<sub>2</sub>-Perturbed Relative Inclination Vector

Figure 42: Relative Inclination Vector Comparison

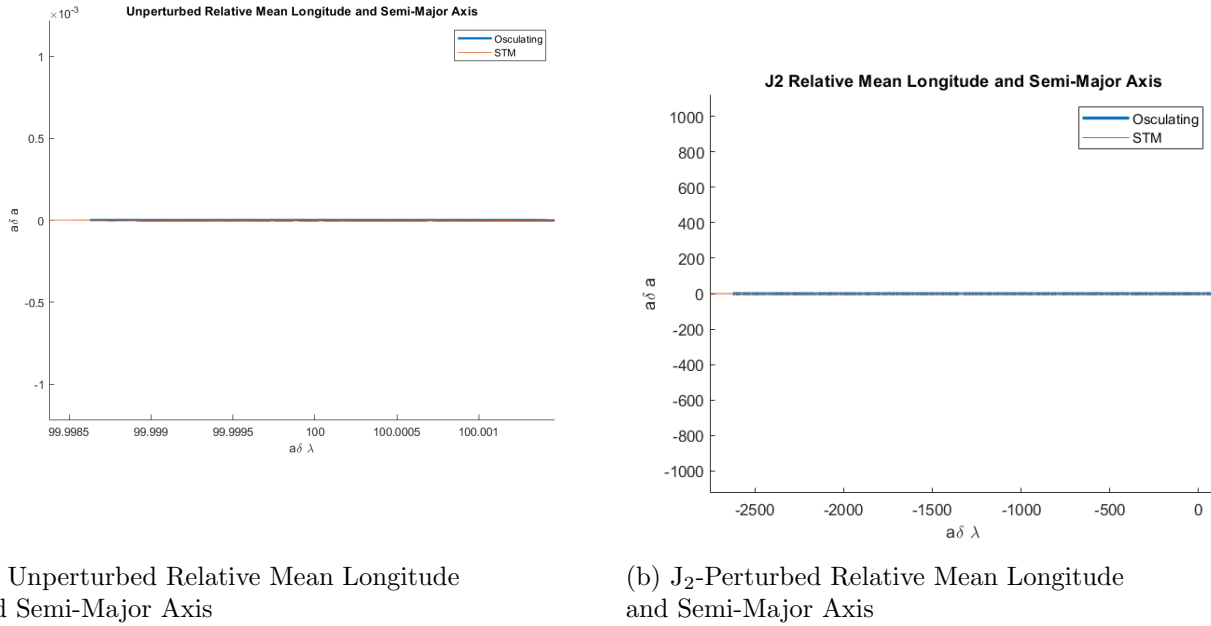


Figure 43: Relative Mean Longitude and Semi-Major Axis Comparison

It is evident from the above plots that, other than an anomaly involving the eccentricity vector, the state transition matrix propagation results coincided very well with the numerical integration.

## 9 Control Law Requirements

By analyzing the dynamics of relative motion and implementing mission-based control laws, the following scenarios of interest are to be examined: (1) formation keeping, and (2) reconfiguration.

In terms of the necessary modes of operation for the formation keeping of Dragon with respect to the ISS, two modes will be analyzed in further detail. Of these modes, the first represents a station-keeping mode which demonstrates precision R-bar arrival at 350 m below the ISS, and the second represents a rendezvous approach to the ISS with a free drift of 10 m from Node 2 Nadir for berthing[6].

### 9.1 R-bar Configuration Mode

To enter the first rendezvous phase of the mission, the Dragon vehicle must go from a separate orbit from the ISS (Drift Orbit A) which is both out of sight and contact from the ISS, to a new orbit which is both in sight and contact (Drift Orbit B). This change in orbit thus makes Dragon an active, or 'chaser,' spacecraft, and will shift the chief/deputy relationship of the relative motion dynamics to adjust the reference (chief) orbit to be that of the ISS. Typically, for maneuvers such as these, the two spacecraft are initially separated by more than 10 kilometers for 1-20 days and must alter its orbit to maintain a separation distance of around one kilometer in order to make radio contact with the station for communications and command verification before approach.

As was used in the analysis of the relative motion dynamics throughout the report, this controls study will begin at Drift Orbit B, where the relative separation distance between the two vehicles is around one kilometer.

In terms of relative orbital elements, this initial condition will be described by the following state:

$$a_c(\delta a, \delta\lambda, \delta e_x, \delta e_y, \delta i_x, \delta i_y) = (-1000, -6781.8, 1.61 \times 10^{-10}, 2.24 \times 10^{-9}, 67.8, 0) \text{ m}$$

Therefore, the first maneuver that the Dragon vehicle must make in order to enter the first operational mode is to go from Drift Orbit B (one kilometer of separation distance) to 350 meters of separation distance (known as 'Proximity Operations A').

In particular, the desired relative orbit in Proximity Operations A is defined in relative orbital elements by the following:

$$a_c(\delta a, \delta\lambda, \delta e_x, \delta e_y, \delta i_x, \delta i_y) = (-300, -6.78, 1.61 \times 10^{-5}, 2.24 \times 10^{-4}, 0, 0) \text{ m}$$

Since this desired position is outside of the ISS's 200 meter Keep-out Sphere (KOS), this maneuver does not need to have incredibly high precision on approach to the one kilometer radial offset. As a result, achieving this desired relative orbit may either take advantage of an impulse-based maneuver scheme over a time span of several orbits using the near-circular reference orbit assumption of the HCW equations, or via a continuous burn via Lyapunov methods for nonlinear continuous formation control is the R-bar constraint is to be given more weight (must be coplanar and have same orbit phase).

Considerations of total  $\Delta V$  used and time taken to reach desired position will be used to form a pareto-optimal solution for R-bar approach.

## 9.2 Rendezvous/Docking Mode

After maneuvering into the R-bar configuration, the Dragon vehicle will enter the ISS'S KOS and hold at a relative distance of 10 meters from the berthing port (Proximity Operations B).

In particular, the desired relative orbit in Proximity Operations B is defined in relative orbital elements by the following:

$$a_c(\delta a, \delta\lambda, \delta e_x, \delta e_y, \delta i_x, \delta i_y) = (-10, 0, 0, 0, 0, 0) \text{ m}$$

For Proximity Operations B, a continuous burn via Lyapunov methods for nonlinear continuous formation control can be implemented to ensure that the approach within the ISS's KOS is controlled and highly accurate. To prevent overshoot and ensure safety regulations are not violated, an additional bang-off controller will be implemented to ensure that the relative vehicle separation never falls below 10 meters. This will require a state estimator that uses relative position knowledge on centimeter order accuracy to ensure that state estimates do not allow any potential violations of safety radii during the close approach. Once at the desired relative state, the dragon vehicle will then deactivate all thrusters and drift as it prepares for the berthing procedure to begin.

## 10 Controller Implementation

In order to perform the aforementioned maneuvers, a combination of impulsive and pseudo-continuous controllers were implemented in the system. In implementation, these controllers have been adapted to

meet the needs of the mission, and therefore may not directly reflect proposed control schemes previously outlined.

Also, in order to implement the  $\delta v$  into the dynamics of the simulation, the  $\delta v$  is converted from RTN frame to ECI, divided by the simulation time step to get a change in acceleration, and then added as a perturbation into the fundamental orbit dynamics equations. Therefore, both controllers outline maneuvers in the RTN frame as derived from a set of ROE, and are converted to be an appropriate input into the system prior to implementation.

## 10.1 Impulsive Reconfiguration

In order to achieve reconfiguration between the various phases of the mission, an impulsive controller was added to make the large scale transfer maneuvers. This maneuver planning in a near-circular orbit took advantage of the inversion of the solution of the HCW equations expressed in terms of quasi-nonsingular ROE's and the closed-form deterministic impulsive maneuvering schemes:

For the single-impulse out-of-plane maneuver:

$$\begin{aligned}\delta v_n &= na \|\delta \mathbf{i}^{\text{man}} - \delta \mathbf{i}\| \\ u_M &= \arctan [(\delta i_y^{\text{man}} - \delta i_y) / (\delta i_x^{\text{man}} - \delta i_x)]\end{aligned}$$

For the double-impulse in-plane maneuver:

$$\begin{aligned}\delta v_{t_1} &= \frac{na}{4} [(\delta a^{\text{man}} - \delta a) + \|\delta \mathbf{e}^{\text{man}} - \delta \mathbf{e}\|] \\ \delta v_{t_2} &= \frac{na}{4} [(\delta a^{\text{man}} - \delta a) - \|\delta \mathbf{e}^{\text{man}} - \delta \mathbf{e}\|] \\ u_{M_1} &= \arctan [(\delta e_y^{\text{man}} - \delta e_y) / (\delta e_x^{\text{man}} - \delta e_x)]\end{aligned}$$

where  $u_{M1} = \tan^{-1}(\frac{\delta e_y}{\delta e_x})$  and  $u_{M2} = u_{M1} + \pi$ . This in-plane maneuver (neglecting burns in the normal direction) was selected primarily since it is the minimum cost solution for formation keeping and will require the least amount of total impulse to achieve the target ROE.

## 10.2 Pseudo-Continuous Formation Control

The continuous controller has been reformatted as a psuedo-continuous controller since the vehicle must remain in drift for most of the flight. Therefore, the continuous controller is an ROE-based discrete-LQR approach that solves for  $\delta v$  changes during the penultimate phase of the mission in 350 meter formation-flying with the ISS. In this phase only is continuous control feasible/permitted, and therefore has been modified accordingly.

From the state transition matrix based upon the relative orbital elements, it is possible to propagate a set of relative orbital elements by utilizing the following transition matrix and use this as the A matrix in the discretized LQR solution:

$$\begin{pmatrix} \delta\dot{a} \\ \delta\alpha \end{pmatrix}_t = \Phi(t - t_0) \begin{pmatrix} \delta\dot{a} \\ \delta\alpha \end{pmatrix}_{t_0}$$

DRAG	KEPLER	SECULAR J <sub>2</sub>
$1$	$0 \quad 0 \quad 0 \quad 0 \quad 0 \quad 0$	
$(t_F - t_0)$	$1 \quad 0 \quad 0 \quad 0 \quad 0 \quad 0$	
$\frac{\nu}{2}(t_F - t_0)^2$	$\nu(t_F - t_0) \boxed{1} \quad 0 \quad 0 \quad 0 \quad \mu(t_F - t_0) \boxed{0}$	
$0$	$0 \quad 0 \quad 1 \quad -\dot{\varphi}(t_F - t_0) \quad 0 \quad 0$	
$0$	$0 \quad 0 \quad \dot{\varphi}(t_F - t_0) \quad 1 \quad 0 \quad 0$	
$0$	$0 \quad 0 \quad 0 \quad 0 \quad 1 \quad 0$	
$0$	$0 \quad 0 \quad 0 \quad 0 \quad 0 \quad \lambda(t_F - t_0) \boxed{1}$	

$$\nu = -\frac{3}{2}n \quad \dot{\varphi} = \frac{3}{2}n\gamma(5\cos^2 i - 1) \quad \mu = -\frac{21}{2}n\gamma \sin 2i \quad \lambda = 3n\gamma \sin^2 i$$

As for the B matrix, the following was implemented:

$$B = \frac{1}{an} \begin{bmatrix} 0 & 2 & 0 \\ -2 & 0 & 0 \\ \sin(u) & 2\cos(u) & 0 \\ -\cos(u) & 2\sin(u) & 0 \\ 0 & 0 & \cos(u) \\ 0 & 0 & \sin(u) \end{bmatrix}$$

where  $u$  is the True Argument of Latitude.

By implementing a discrete-LQR function to solve the Riccati equations given A, B, Q = 0.01I<sub>6</sub>, and R = 100I<sub>3</sub>, a gain matrix K is produced. From here, the desired  $\delta v$  can be expressed as:

$$\delta v = -K(ROE - ROE_{desired})$$

For the purposes of the mission, these  $\delta v$ 's are only applied when in the 350 meter drift phase of the mission.

### 10.3 Controller Simulation Results

In order to meet the primary mission goals, the focus of the simulation was to ensure that the vehicle followed a strict set of  $a\delta a$  magnitudes from 1000 meters to 350 meters to 10 meters. This behavior would ensure that the vehicle was in the appropriate distance for communications and rendezvous.

The following plot shows the results of the six ROE over the span of the entire mission, covering both scheduled maneuvers:

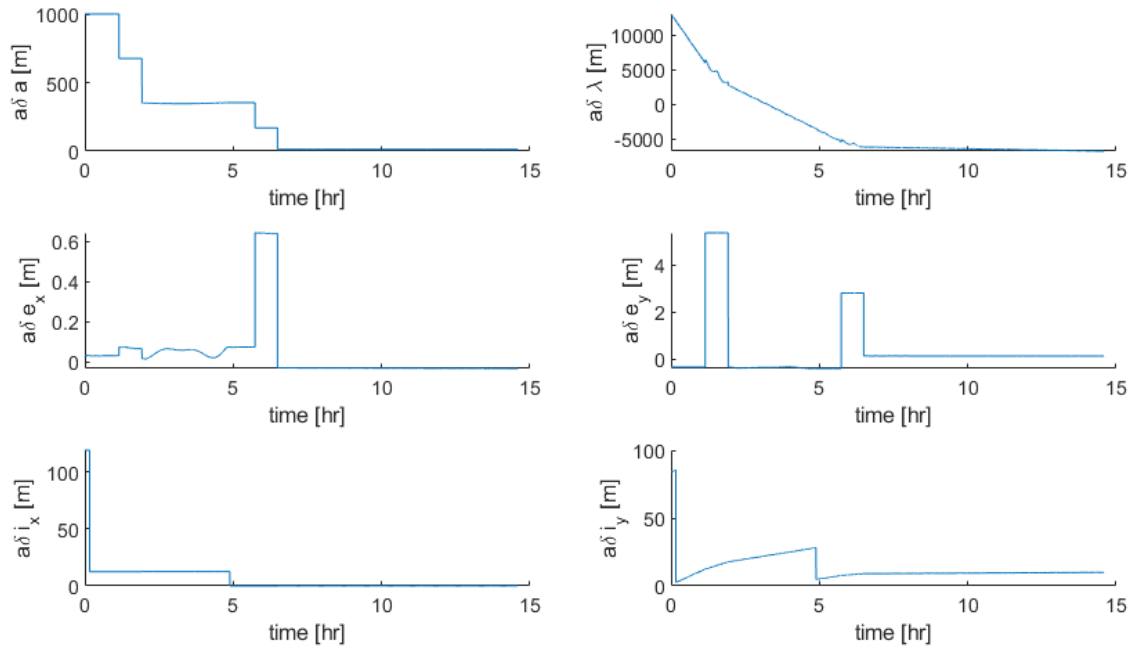
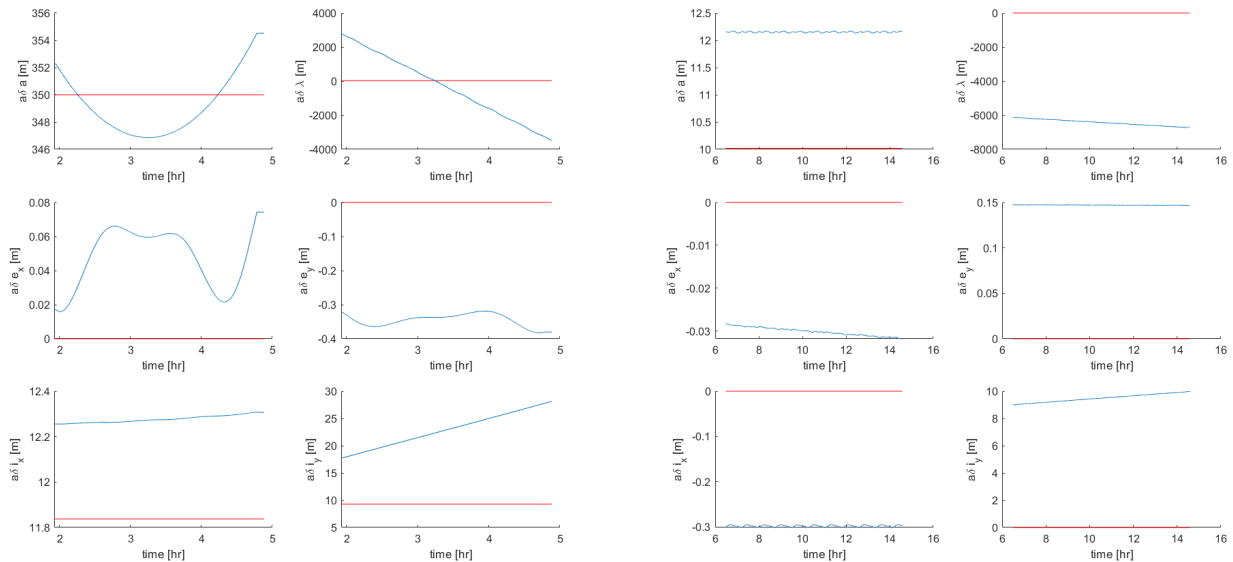


Figure 44: ROE over Mission Duration

For a better sense of what the system looked like during the duration of each phase, the following plot shows true ROE state (blue) overlaid on the desired ROE state (red):



(a) 350m Drift Phase ROE

(b) 10m Drift Phase ROE

Figure 45: True ROE vs Desired ROE for Both Mission Phases

From this plot, it is easy to see that the vehicle holds its relative orbital elements to within 5 meters in all elements other than  $\delta\lambda$  due to a secular drift induced over time.

In the RTN frame, the relative position of the vehicle can be described by the following plot with the first phase in red and the second phase in blue:

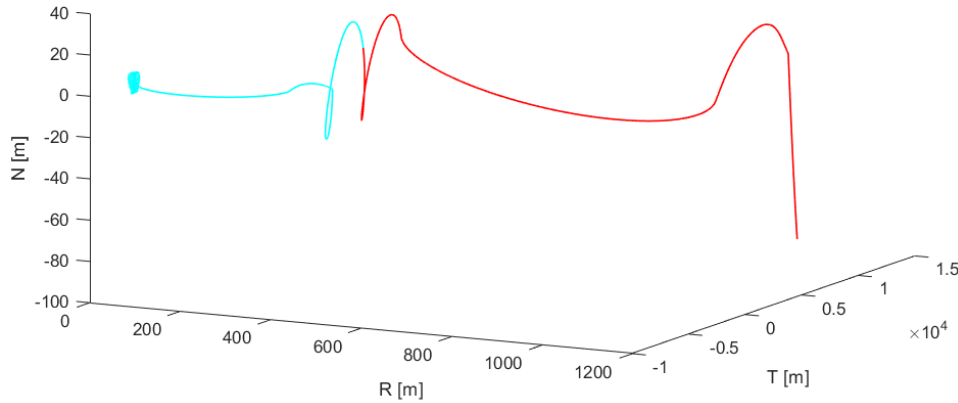


Figure 46: ISS Rendezvous Mission Profile in the RTN Frame

It is clear to see that the vehicle starts about 1 kilometer radially from the ISS with both nonzero normal and tangential displacement, but reaches bounded periodic motion around 10 meters in the radial direction with zero normal and tangential displacement, suggesting that the impulsive schemes were successful.

By taking the norm of the RTN at each timestep, relative distance can be plotted over time, as follows:

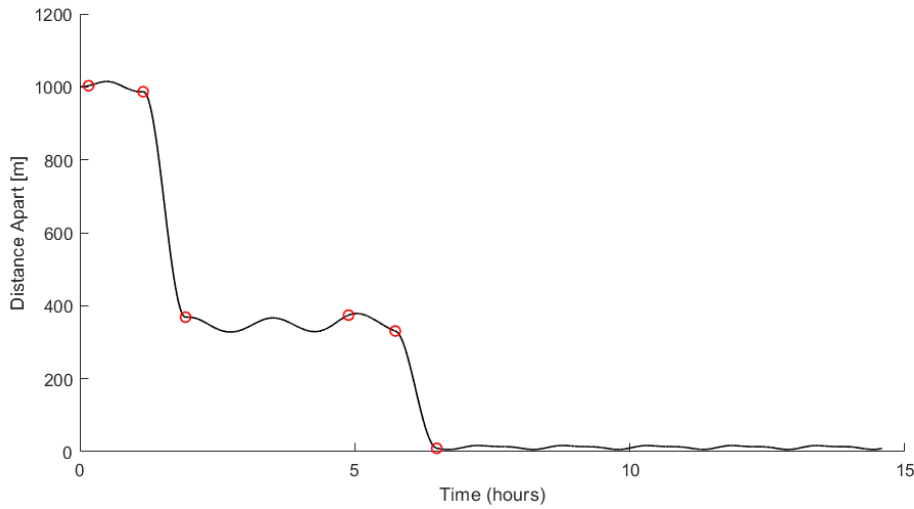
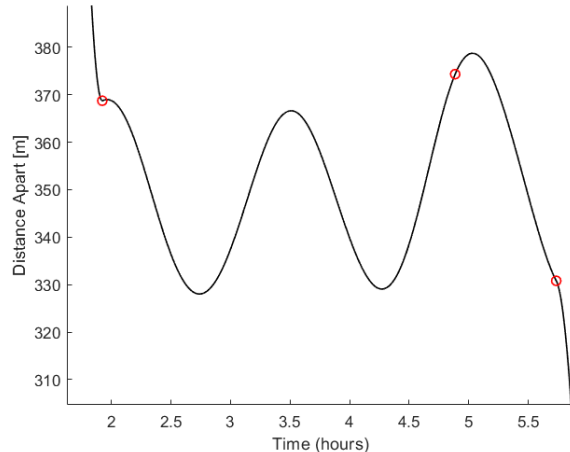


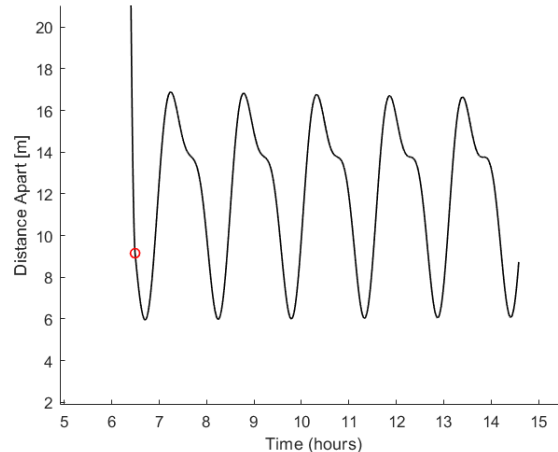
Figure 47: Relative Range over Mission Duration

Viewing the range individually at each phase provides a better sense of oscillation around the desired

range as such:



(a) 350m Drift Phase Range



(b) 10m Drift Phase Range

Figure 48: Individual Drift Phase Ranges

From here, it is clear that the vehicle maintains all distance requirements on the meter level for each mission, and therefore was successful.

As for the total amount of  $\delta v$  used in the mission, the following plot shows the total  $\delta v$  consumption through the duration of the mission:

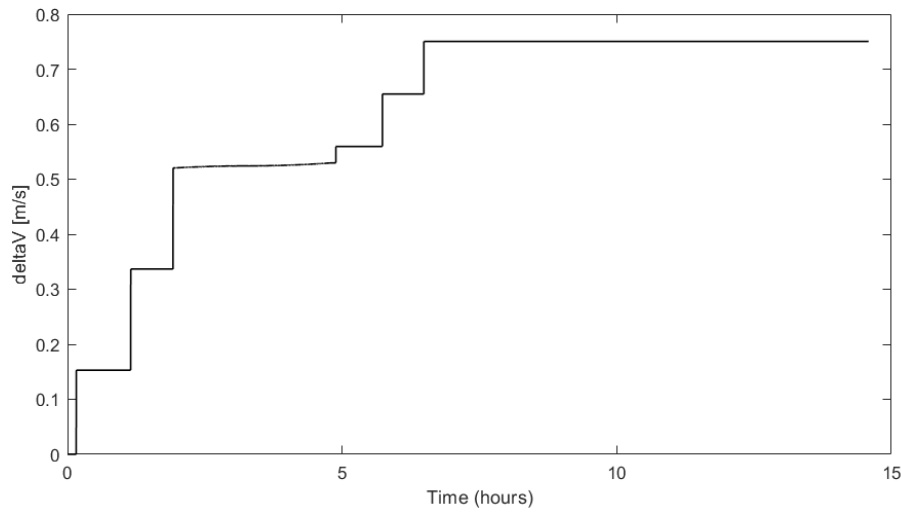


Figure 49: Relative Range over Mission Duration

From this chart, it is clear the the impulsive maneuvers carry much more significance over the total propellant consumption than the pseudo-continuous controller, as the continuous controller is operating around formation-flying requirements on the 1-20 meter level, and the impulsive maneuvers are making 300-700 meter transfers.

## 11 Navigation System Design

### 11.1 Relative State Representation

As this navigation problem encapsulates the rendezvous approach of two near-circular orbits, the HCW equations will be utilized on first approach to the ISS in phase one of the transfer/capture. Therefore, the set of quasi-nonsingular relative orbital elements used to define the two phases will be converted into relative position and velocity.

### 11.2 State Prediction Model

From a state defined by relative position and velocity, the following state prediction model can be implemented:

$$\dot{\mathbf{x}}(t) = \begin{bmatrix} 0 & 1 & 0 & 0 & 0 & 0 \\ 3n^2 & 0 & 0 & 2n & 0 & 0 \\ 0 & 0 & 0 & 1 & 0 & 0 \\ 0 & -2n & 0 & 0 & 0 & 0 \\ 0 & 0 & 0 & 0 & 0 & 1 \\ 0 & 0 & 0 & 0 & -n^2 & 0 \end{bmatrix} \mathbf{x}(t)$$

$$\mathbf{x}(t) = [x \ \dot{x} \ y \ \dot{y} \ z \ \dot{z}]^T$$

### 11.3 Covariance Update Matrices

The associated linearized dynamics model used in the EKF covariance update will have the following state transition matrix  $\Phi$  (the HCW transition matrix):

$$\mathbf{e}^{At} = \begin{bmatrix} 4 - 3c_{nt} & 0 & 0 & \frac{s_{nt}}{n} & \frac{2}{n} - \frac{2c_{nt}}{n} & 0 \\ -6nt + 6s_{nt} & 1 & 0 & -\frac{2}{n} + \frac{2c_{nt}}{n} & \frac{4s_{nt}}{n} - 3t & 0 \\ 0 & 0 & c_{nt} & 0 & 0 & \frac{s_{nt}}{n} \\ 3ns_{nt} & 0 & 0 & c_{nt} & 2s_{nt} & 0 \\ -6n + 6nc_{nt} & 0 & 0 & -2s_{nt} & -3 + 4c_{nt} & 0 \\ 0 & 0 & -ns_{nt} & 0 & 0 & c_{nt} \end{bmatrix}$$

Note that the state vector for  $\Phi$  is:

$$\mathbf{x}(t) = [x \ y \ z \ \dot{x} \ \dot{y} \ \dot{z}]^T$$

Also, for dynamic control of the system, the following RTN coordinate dynamics provide the control input matrix,  $\mathbf{B}$ :

$$\dot{\mathbf{x}} = A \begin{bmatrix} R \\ \dot{R} \\ T \\ \dot{T} \\ N \\ \dot{N} \end{bmatrix} + B \begin{bmatrix} \mathbf{a}_R \\ \mathbf{a}_T \\ \mathbf{a}_N \end{bmatrix}$$

$$A = \begin{bmatrix} 0 & 1 & 0 & 0 & 0 & 0 \\ 3n^2 & 0 & 0 & 2n & 0 & 0 \\ 0 & 0 & 0 & 1 & 0 & 0 \\ 0 & -2n & 0 & 0 & 0 & 0 \\ 0 & 0 & 0 & 0 & 0 & 1 \\ 0 & 0 & 0 & 0 & -n^2 & 0 \end{bmatrix}, \quad B = \begin{bmatrix} 0 & 0 & 0 \\ 1 & 0 & 0 \\ 0 & 0 & 0 \\ 0 & 1 & 0 \\ 0 & 0 & 0 \\ 0 & 0 & 1 \end{bmatrix}$$

## 11.4 Sensor Specifications

For the purpose of on-orbit navigation, Dragon has a suite of Inertial Measurement Units (IMU), GPS Systems, and Star Trackers. Both the IMUs and star trackers have an accuracy of  $0.004^\circ$  or smaller. The threshold of attitude control is also  $0.012^\circ$  on each axis in station-keeping Mode [4]. Once the vehicle reaches the approach orbit within the KOS of the ISS, Dragon initializes proximity sensors (LIDARs and thermal imagers) and converges a solution for range and range rate before proceeding[6].

From both the GPS and LIDAR sensors, a noisy range measurement will be returned to produce measurements of relative position and velocity. On the other hand, the star trackers return quaternion measurements, they are used solely for attitude determination and control and will not be included in navigation control.

## 12 Navigation System Implementation

In place of the Extended Kalman Filter (EKF), an Unscented Kalman Filter (UKF) was implemented to be a better fit for the mission. Since the allotted window for convergence on the continuous burn in the system is only about a single orbital period, a better filter for the mission requires fast convergence times, giving the UKF the advantage over the EKF since it approximates the nonlinearities better than an EKF.

With the controller turned off on the system, the two vehicles were allowed to drift over several orbits with the following initial condition:

$$a_c(\delta a, \delta \lambda, \delta e_x, \delta e_y, \delta i_x, \delta i_y) = (-1000, -6781.8, 1.61 \times 10^{-10}, 2.24 \times 10^{-9}, 67.8, 0) \text{ m}$$

As for the UKF, the filter takes in GPS measurements in the form of noisy position measurements and converts the relative position estimate into an ROE. The state being estimated is the ROE with a propagation provided by the State Transition Matrix that served as the A matrix in the discrete-LQR implementation.

For initial covariance, a standard deviation of 2 meters across the diagonal. This represents a fairly good initial estimate of the ROE, but the convergence rate is nearly instantaneous, so the estimate was reduced to assist in plotting. Both Q and R were set to be  $0.1I_6$  for the filter.

The following plot shows the True vs Measure ROE within the UKF:

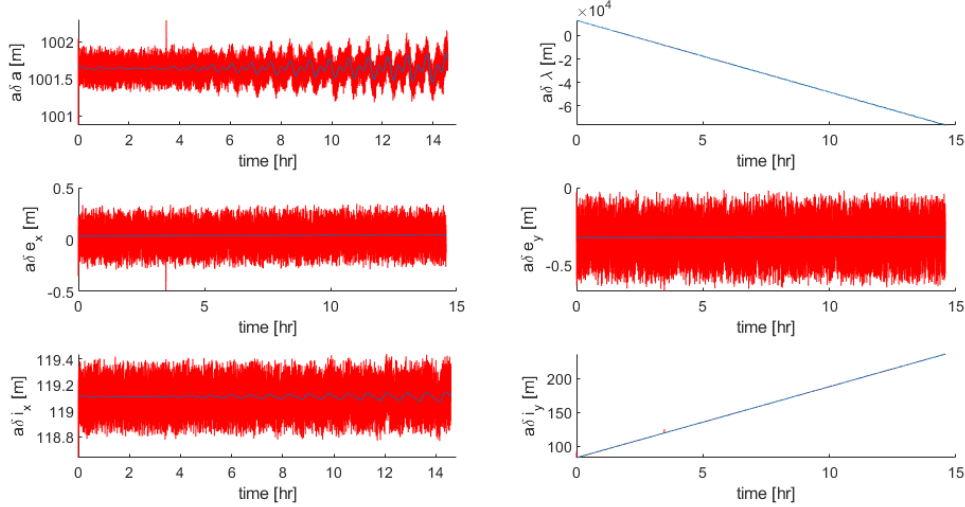


Figure 50: True vs Measure ROE

From this plot, it can be seen that the noise on the system only perturbed the estimate on the order of a centimeter. The standard deviation of the error is shown in the following plot to  $3\sigma$  as upper and lower bounds:

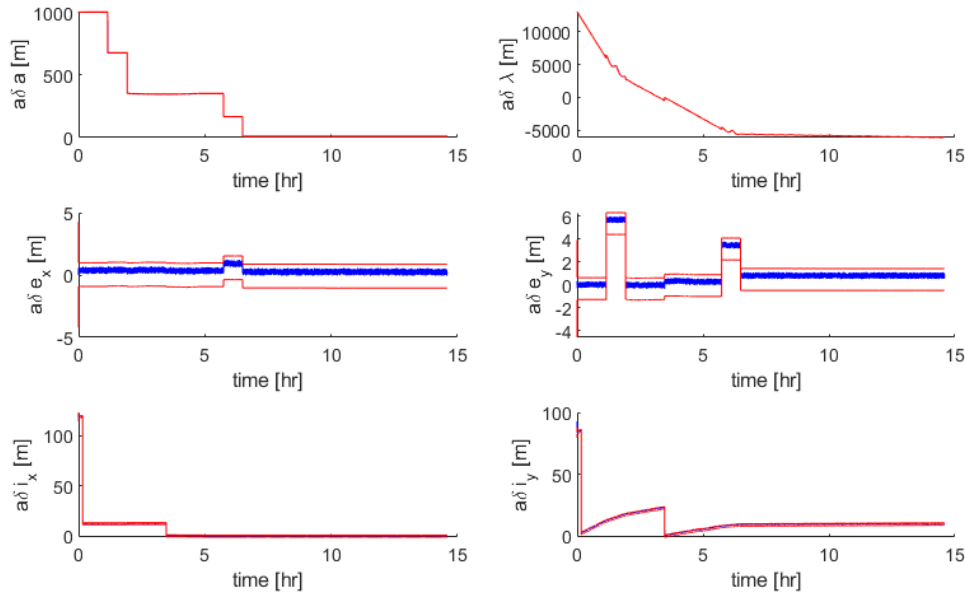


Figure 51:  $3\sigma$  Estimate Bounds

From here, it is possible to calculate when the system reaches its minimum standard deviation (assumed to be the convergence point) at around 5 minutes, or 60 iterations of the UKF.

The following plot shows the pre-fit (blue) and post-fit (red) residuals of the UKF:

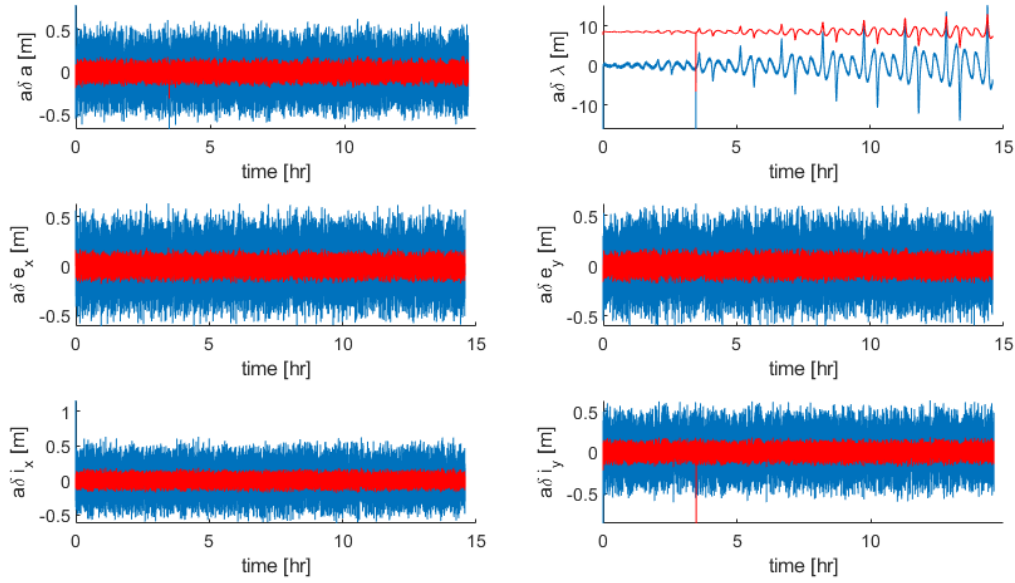


Figure 52: Pre-fit and Post-fit Residuals

With this plot of the residuals, it can be seen that the only error is that the post-fit residual of  $\delta\lambda$  is 10 meters offset, but otherwise remains significantly smaller than the pre-fit error. With these results, the next step is to integrate the filter into the system as an estimate state input to the controller.

## 13 Filter Integration

As the final simulation of the report, the UKF was modified to provide state knowledge to the impulsive controller. This decision was made by simply remembering the difference in influence between the  $\delta v$  maneuvers of the two controllers. Since the impulsive controller is the dominant force in the simulation, it would be affected the most by a noise estimate of state (especially since the magnitudes of the burns are mapped specifically to a precise set of ROE).

### 13.1 Unfiltered Noisy State Control

Prior to implementing the filter, the control state input ROE was first subjected to Gaussian white noise on the same order as the covariance of the UKF implementation.

The following results show the propagation of the ROE under the influence of a noisy state in the impulsive controller without the UKF for comparison:

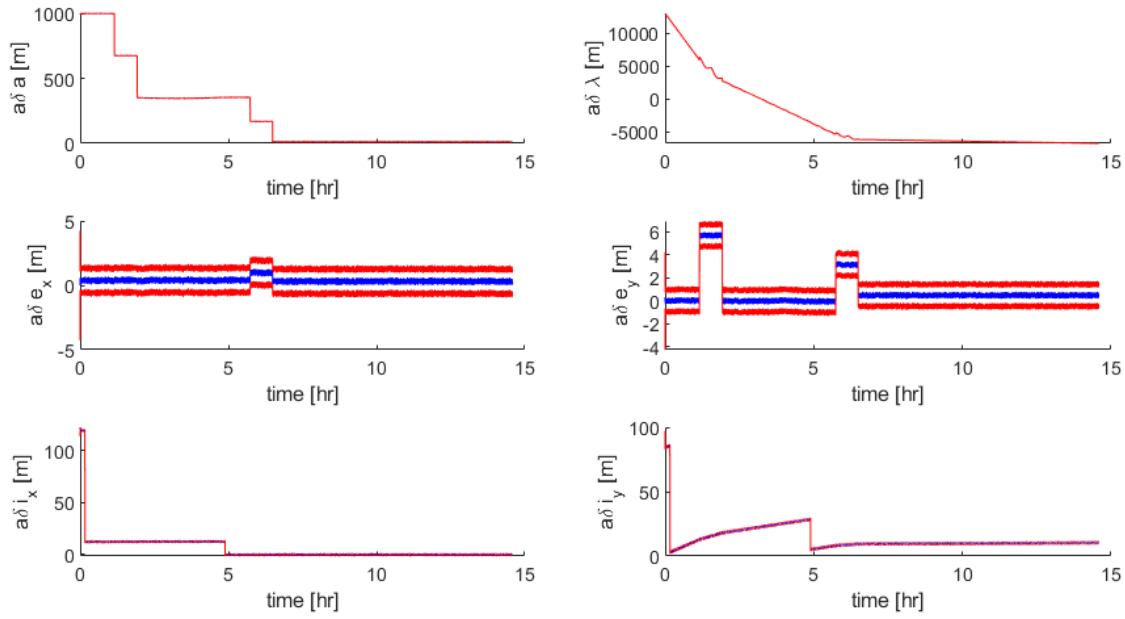


Figure 53: Noisy ROE Impulsive Control

With a relatively small variance of the Gaussian white noise added onto the state to the controller, it can be seen that the system holds to a recognizably similar ROE profile than it does without the noise.

With the noise in the system, the spacecraft undergoes the following range profile with the ISS:

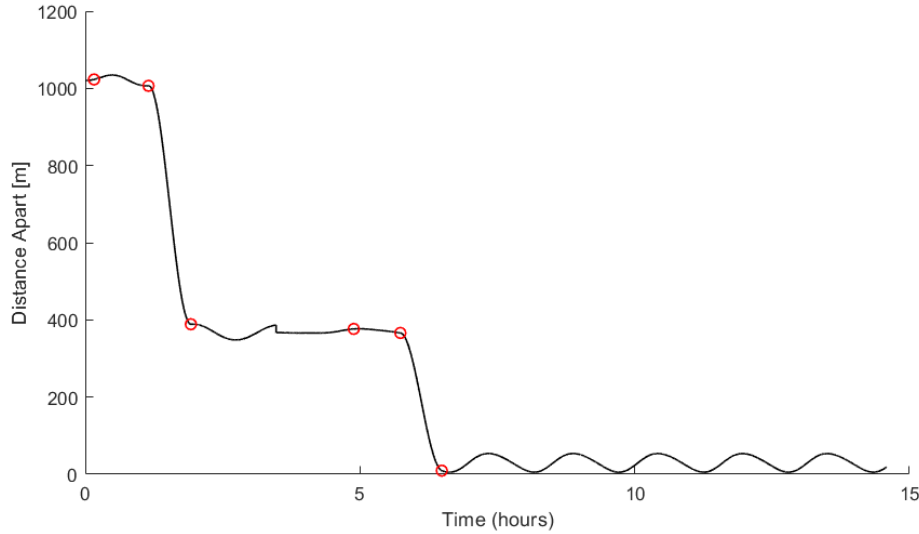


Figure 54: Range Profile via Unfiltered Noise

By focusing on the individual timescales of each phase, the following plots can be analyzed:

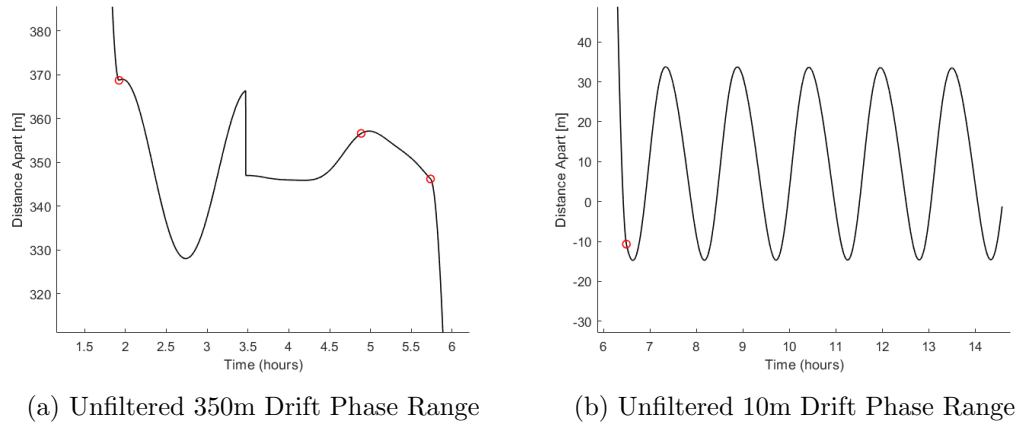
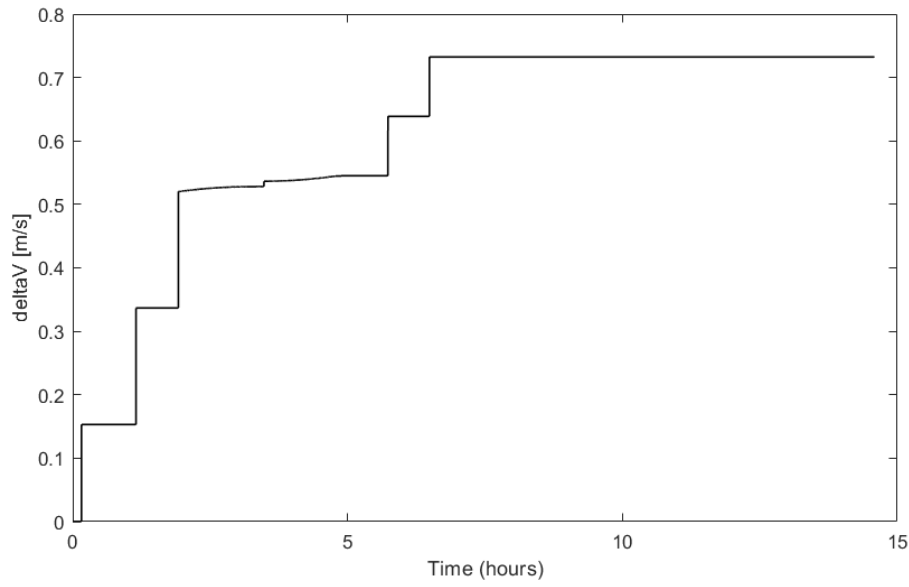


Figure 55: Individual Unfiltered Drift Phase Ranges

As it can be seen in the 350m drift phase, a large perturbation of the pseudo-continuous discrete-LQR controller causes the system to aggressively correct when the state is not known, causing an overshoot. When it is time for the system to make its final impulsive maneuver to 10m for proximity operations, the system overshoots again and causes the range to exceed 0m (suggesting that the vehicle collided with the ISS).

Unsurprisingly, even with the  $\delta v$  maneuver in the 350m drift phase, the overall  $\delta v$  stays within the same order of magnitude as without the noise as shown in the following figure:

Figure 56: Filtered  $\delta v$  Consumption

Of note in the previous graph is the influence of the continuous controller on the overall fuel consumption, and while it is small, is non-negligible as is was before.

### 13.2 Filtered Noisy State Control

Using the UKF to feed the control law its state input yields significantly improved results. Whereas the ROE estimates yield similar results to the unfiltered results, the pre-fit and post-fit residuals show a significant improvement in resolution (as shown in the following two figures):

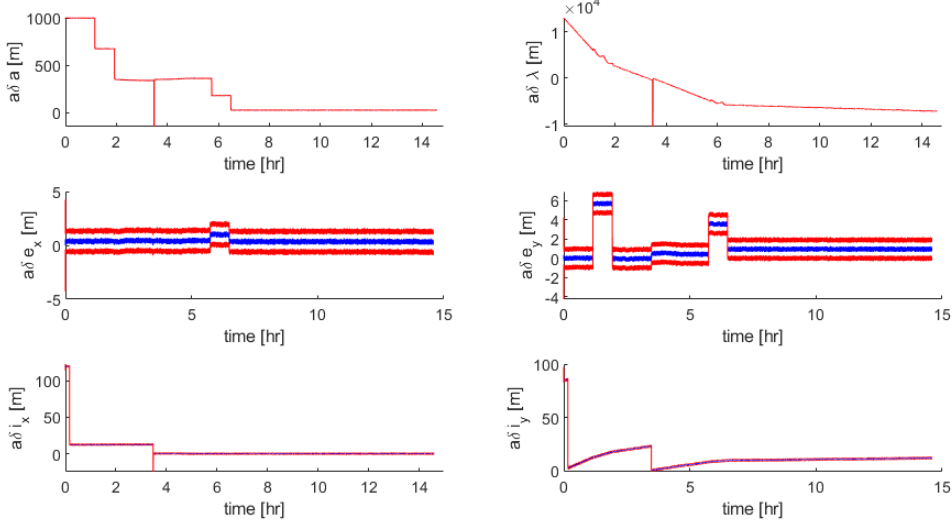


Figure 57: Filtered ROE Control

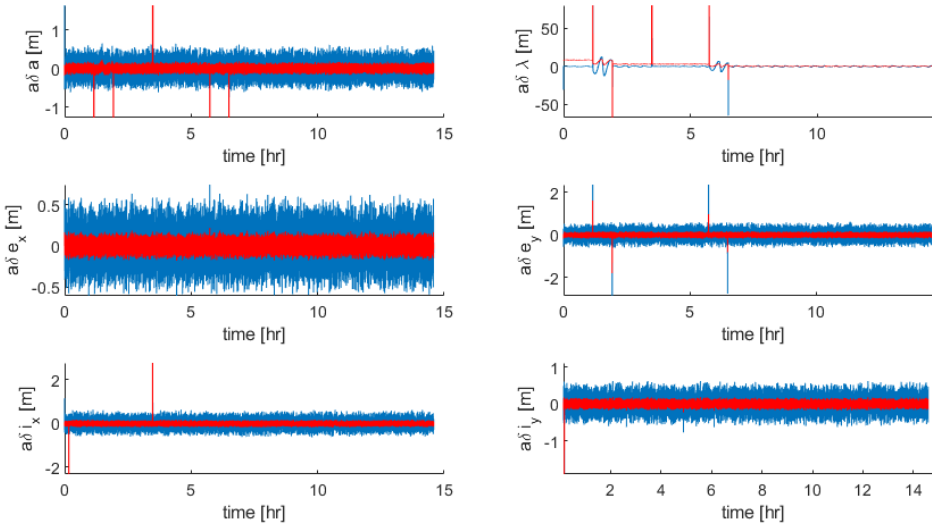


Figure 58: Filtered ROE Residuals

By visualizing the range between the two craft over the duration of the mission, the following plot was produced:

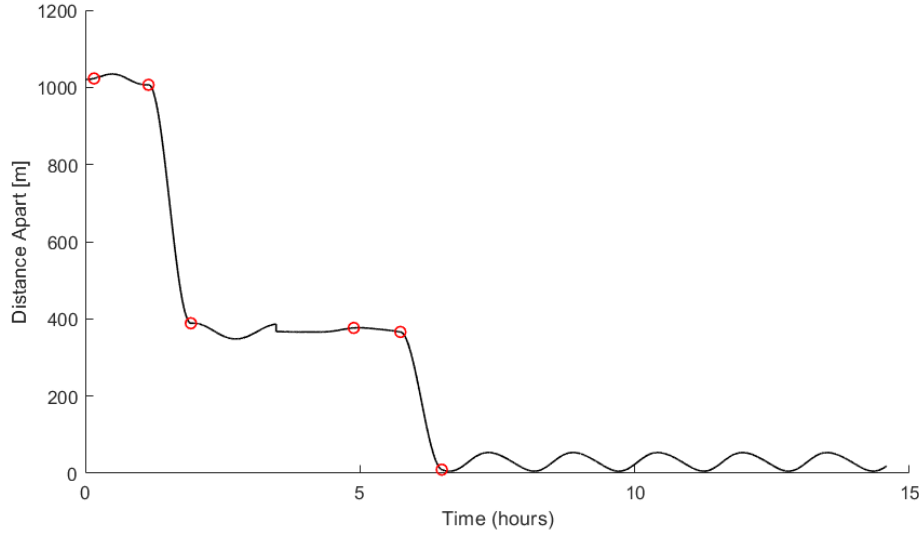
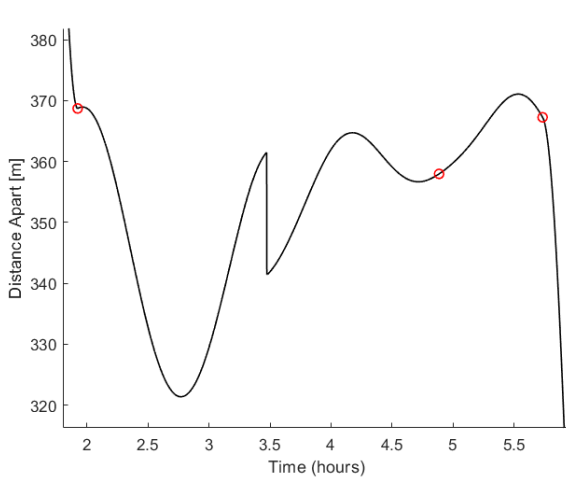
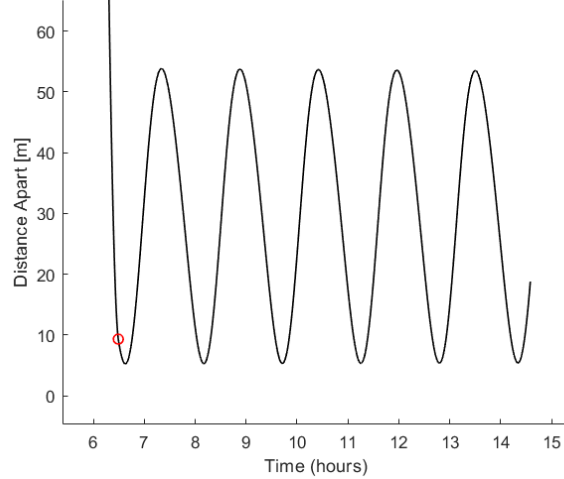


Figure 59: Range Profile via Unfiltered Noise

The individual phase ranges can also be extracted from this plot as such:



(a) Unfiltered 350m Drift Phase Range



(b) Unfiltered 10m Drift Phase Range

Figure 60: Individual Unfiltered Drift Phase Ranges

Once again, it can be seen in the 350m drift phase that a perturbation of the pseudo-continuous discrete-LQR controller causes the system to aggressively correct when the state is not known, but the state is soon corrected and allows for a closer burn to what is seen in the 10m phase. Unlike the unfiltered profile, this mission does not crash directly into the bottom of the ISS, but instead remains in a periodic drift from 50m to 10m, and remains in the operational zone for ISS berthing procedures for approximately 45 minutes.

The  $\delta v$  consumption of this filtered mission not only shows a correction for the large burn (which is now of smaller magnitude), but it also completes the mission in the same amount of total propellant as seen

in the following figure:

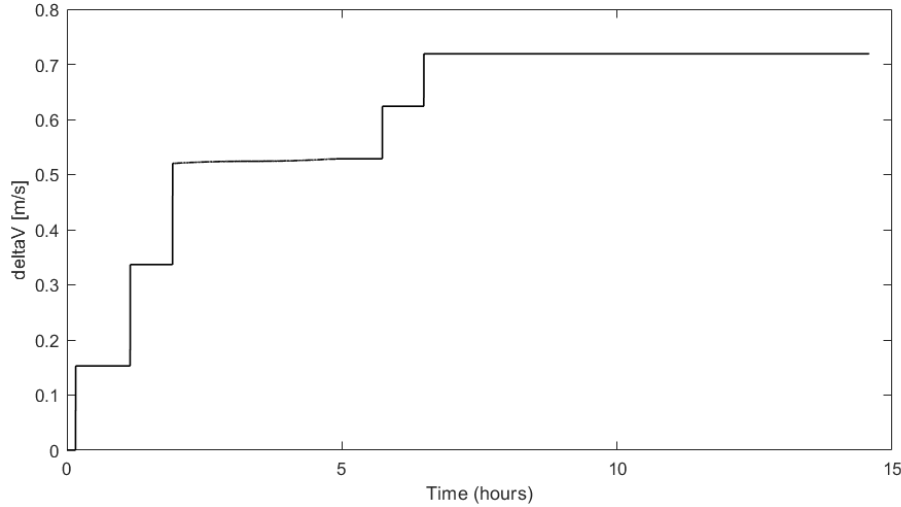


Figure 61: Unfiltered  $\delta v$  Consumption

Overall, the UKF performed as expected, allowing the nonlinearities of the impulse and continuous maneuvers to be accounted for, all while reducing the error in state estimate of the vehicle, allowing for more accurate burns. While the filter did not perform nearly as well as the noise-free simulation results, careful tuning of LQR gains and UKF covariance would allow for near-nominal results.

## 14 Conclusions and Future Work

The primary concern of the entire mission profile was the availability of control and the window of control operation, not the amount of propellant. Since the mission window per phase was relatively small (2-3 hours), it was infeasible to implement a controller that would instantly converge on noisy measurements. Therefore, the pseudo-continuous controller was fashioned to provide frequent, but much smaller, impulsive maneuvers using discrete-LQR from the ROE state transition matrix. The only issue was that no state correction could be done once entering the final (10 meter) proximity operations phase, as it is within the KOS of the ISS and must remain in a drift. This makes it difficult to stabilize oscillatory motion around the rendezvous port of the ISS, and therefore was assumed to be 'stable' within some tolerance - that being the window of time it was within reach of the robotic manipulator used for berthing. While the UKF created a stable drift for the vehicle on approach to proximity operations, a more feasible solution may have been to set the vehicle into a transfer orbit that would provide a long-periodic effect that would cause the vehicle to be within 10 meters for much longer, but with less stability. The long-period relative position to the ISS would be suitable for the mission and not require the final correction burn within 10 meters as it does in its current state.

Future work would investigate different configurations of impulse/continuous burns to achieve the desired ROE's without  $\delta\lambda$  drifting.

# Appendices

## A Two Line Element Sets (TLE)

DRAGON CRS14

```
1 43267U 18032A    18105.51925310 +.00002699 +00000-0 +47756-4 0  9996
2 43267 051.6438 331.1221 0001905 355.8915 076.9789 15.54265438108777
```

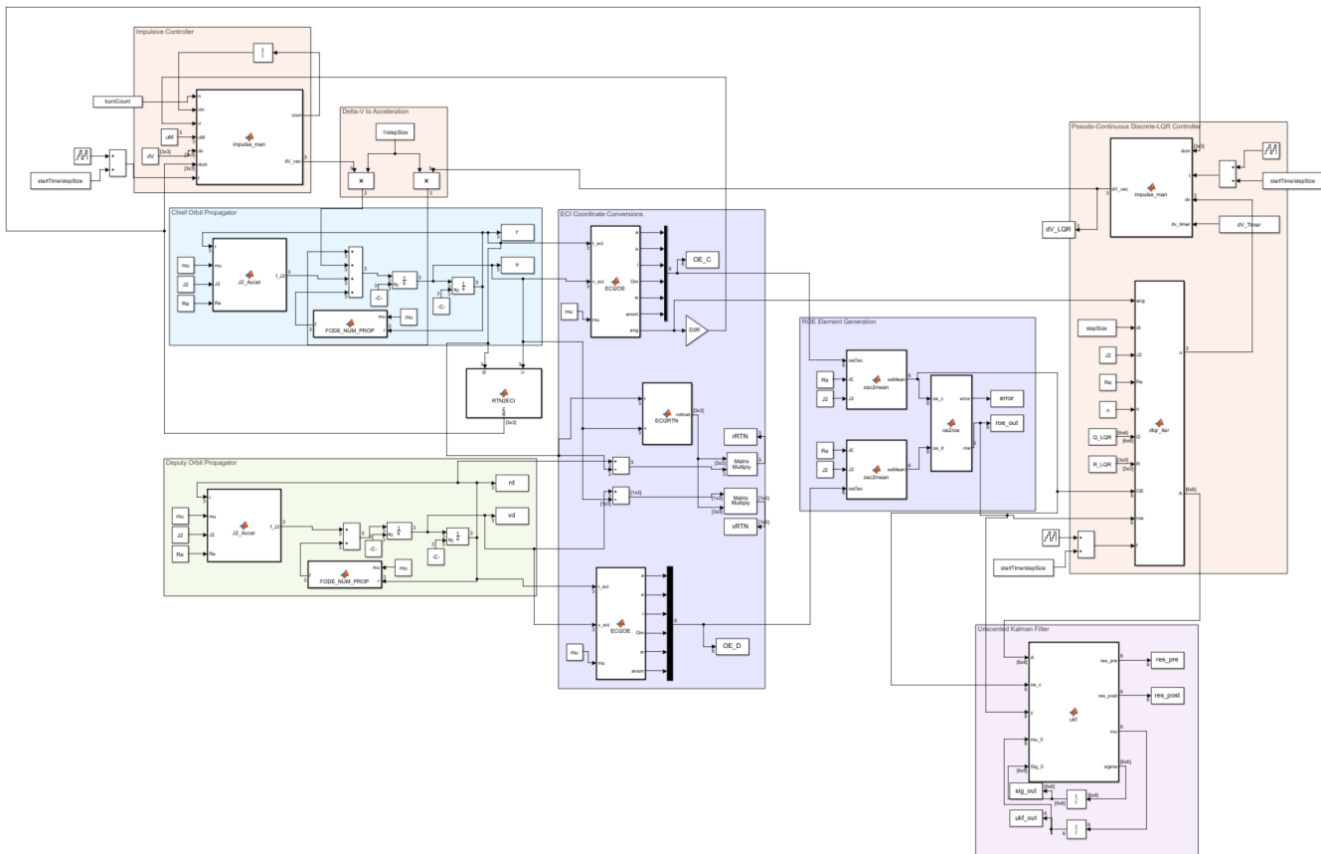
TINTIN A

```
1 43216U 18020B    18106.53254881 .00002260 00000-0 11029-3 0  9995
2 43216 97.4562 114.6986 0016194 91.5260 268.7829 15.19214506 8037
```

TINTIN B

```
1 43217U 18020C    18105.93439396 -.00000056 +00000-0 +60291-6 0  9995
2 43217 097.4630 114.1702 0016101 097.6203 262.6859 15.19282153007945
```

## B Simulink Control and Filter Model



## References

- [1] K. Alfriend, S. Vadali, P. Gurfil, J. How, and L. Breger, *Spacecraft Formation Flying: Dynamics, Control, and Navigation*. Elsevier Astrodynamics Series, 2010.
- [2] C. Stephen (2 April 2018). "Launch Log". Spaceflight Now. Archived from the original on 5 April 2018.
- [3] C. Stephen (4 April 2018). "Dragon cargo capsule reaches space station for second time". Spaceflight Now. Retrieved 4 April 2018.
- [4] Spaceflight101 (n.d.). Dragon - Cargo Version. Retrieved April 14, 2018, from <http://spaceflight101.com/spacecraft/dragon/>
- [5] Spaceflight101 (n.d.). Dragon SpX-14 Cargo Overview. Retrieved April 23, 2018, from <http://spaceflight101.com/dragon-spx14/cargo-overview/>
- [6] "Overview: SpaceX CRS-14 Mission" (PDF). NASA. Retrieved 4 April 2018.
- [7] Grush, Loren (15 February 2018). "SpaceX is about to launch two of its space Internet satellites: the first of nearly 12,000". The Verge. Retrieved 16 February 2018.
- [8] de Selding, Peter B. (2016-10-05). "SpaceX's Shotwell on Falcon 9 inquiry, discounts for reused rockets and Silicon Valley's test-and-fail ethos". SpaceNews. Retrieved 2016-10-08.
- [9] Gates, Dominic (16 January 2015). "Elon Musk touts launch of 'SpaceX Seattle'". Seattle Times. Retrieved 19 January 2015.
- [10] Messier, Doug (2017-03-03). "SpaceX Wants to Launch 12,000 Satellites". Parabolic Arc. Retrieved 2018-01-22.
- [11] Musk, Elon (22 February 2018). "First two Starlink demo satellites, called Tintin A & B, deployed and communicating to Earth stations (video)". Twitter. Retrieved 22 February 2018.